HOKKAIDO UNIVERSITY

DOCTORAL THESIS

Exploring Non-adiabatic Molecular Dynamics: Insights into the Dependence on Diabatic and Adiabatic Potential Energy Surfaces and Applications to Excited-State Reaction Dynamics

---

Satoi Wada

A thesis submitted to

the Graduate School of Chemical Sciences and Engineering

in fulfillment of the requirements for the degree of

DOCTOR OF PHILOSOPHY

Mar. 2024

Contents

I General Introduction **1**

II Intersystem crossing dynamics based on spin-pure and spin-mixed potential energy surfaces with Tully's fewest switches algorithm **15**

2.1 Introduction 16

2.2 Tully's fewest switches algorithm 19

2.3 Results and Discussions 22

2.3.1 Geometries of equilibrium structure and MESX structure 23

2.3.2 Potential energy curves for spin-pure and spin-mixed states 25

2.3.3 Spin-orbit coupling and non-adiabatic coupling 28

2.3.4 Tully's fewest switches (TFS)-SH-AIMD simulations using spin-pure/spin-mixed states 30

2.4 Conclusion 38

III Intersystem crossing dynamics based on spin-pure and spin-mixed potential energy surfaces with Zhu-Nakamura global switching algorithm **40**

3.1 Introduction 41

3.2 Zhu-Nakamura Global Switching algorithm 44

3.3 Results and Discussions 47
3.3.1 Time evolution of the fraction of the triplet state of trajectories . . . 48
3.3.2 Distribution of the number of surface hopping against energy difference 51
3.3.3 ISC probability 52
3.4 Conclusion 53

IV Excited-State Intramolecular Proton Transfer and subsequent dynamics of *ortho*-nitrophenol 56
4.1 Introduction 56
4.2 Computational Details 59
4.3 Results and Discussion 59
4.3.1 Franck-Condon excited states 61
4.3.2 Excited-State Intramolecular Proton Transfer pathway 63
4.3.3 Minimum energy structure on the conical intersections 66
4.3.4 Non-adiabatic Molecular dynamics 68
4.4 Conclusion 79

V General Conclusion 81

Bibliography 83

Acknowledgement 108

Chapter I

General Introduction

Light-induced phenomena and their use are found not only nature, but also in a wide range of fields such as science, engineering, and medicine. For example, photosynthesis and vitamin D synthesis, solar cells and light-emitting diodes (LED), phototherapy and cell imaging. On the atomic scale, dissociation, isomerization, and/or redox, etc. of molecules occur. They can also occur in thermal reactions, but the mechanism is often quite different in photoreactions. A molecule interacting with light is excited to an electronic excited state and then, releases the excess energy through one or both of those two processes. One is the radiative process, in which the molecule relaxes from the electronically excited state to the ground state, releasing energy as light in the form of fluorescence or phosphorescence emission. The other is the non-radiative process, in which the molecule relaxes to the ground state via a non-adiabatic transition while converting electronic energy to translational, rotational, and/or vibrational energy.

The non-adiabatic transition occurs efficiently in regions where multiple adiabatic potential energy surfaces are energetically close to each other. Landau [1] and Zener [2] are very well known for their pioneering works on non-adiabatic transitions in 1932. Each of

them independently proposed an formula to calculate a non-adiabatic transition probability at potential energy crossing. Now it is known as the Landau-Zener formula presented here.

$$P^{\mathrm{LZ}} = \exp\left(-2\pi \frac{\left|V_{12}\right|^2}{\mathrm{v}\left|F_1 - F_2\right|}\right) \tag{1.1}$$

This Landau-Zener formula is still often used, but to elucidate the origin of photophysical and photochemical properties, it is necessary not only to evaluate a non-adiabatic transition probability, but also to correctly simulate the entire dynamics, including deterministic processes in excited states that occur during femtosecond or picosecond order.

A complete description of an isolated molecular system in a non-relativistic manner is given by the time-dependent Schrödinger equation [3]:

$$i\hbar \frac{\partial}{\partial t} \Psi(\mathbf{r}, \mathbf{R}, t) = \hat{H} \Psi(\mathbf{r}, \mathbf{R}, t) \tag{1.2}$$

with the non-relativistic molecular Hamiltonian:

$$\begin{aligned}
\hat{H} \;=\; & -\sum_{i}^{n} \frac{\hbar^2}{2m_e} {\nabla_i}^2 && -\sum_{A} \frac{\hbar^2}{2M_A} {\nabla_A}^2 \\
& + \sum_{i,j} \frac{e^2}{4\pi\epsilon_0 |\mathbf{r}_j - \mathbf{r}_i|} && + \sum_{i,A} \frac{-Z_A e^2}{4\pi\epsilon_0 |\mathbf{R}_A - \mathbf{r}_i|} && + \sum_{A,B} \frac{Z_A Z_B e^2}{4\pi\epsilon_0 |\mathbf{R}_B - \mathbf{R}_A|} \\
=\; & \hat{T}_e(\mathbf{r}) && + \hat{T}_N(\mathbf{R}) \\
& + \hat{V}_{ee}(\mathbf{r}) && + \hat{V}_{eN}(\mathbf{r}, \mathbf{R}) && + \hat{V}_{NN}(\mathbf{R})
\end{aligned} \tag{1.3}$$

including kinetic energy oprators for nuclei and electrons ($\hat{T}_e$ and $\hat{T}_N$) and Coulomb interaction operators of electron-electron ($\hat{V}_{ee}$), electron-nucleus ($\hat{V}_{eN}$) and nucleus-nucleus ($\hat{V}_{NN}$). The total molecular wavefunction is expanded in terms of the time-independent electronic

wavefunction, so called the Born-Huang expansion [4] as follows:

$$\Psi(\mathbf{r},\mathbf{R},t) = \sum_I \Phi_I(\mathbf{r};\mathbf{R})\, X_I(\mathbf{R},t) \tag{1.4}$$

where the subscript I denotes the electronic state and $\Phi(\mathbf{r};\mathbf{R})$ is an electronic wavefunction. Then, $X_I(\mathbf{R},t)$ is a nuclear wavefunction associated with the Ith electronic state. The electronic wavefunctions are obtained from time-independent electronic Schrödinger equation for a given nuclear configuration:

$$\begin{aligned} \hat{H}^e(\mathbf{r},\mathbf{R})\,\Phi_I(\mathbf{r};\mathbf{R}) &= E_I \Phi_I(\mathbf{r};\mathbf{R}) \\ \hat{H}^e(\mathbf{r},\mathbf{R}) &= \hat{T}_e(\mathbf{r}) + \hat{V}_{ee}(\mathbf{r}) + \hat{V}_{eN}(\mathbf{r},\mathbf{R}) \end{aligned} \tag{1.5}$$

Inserting Eq. (1.4) into the time-dependent Schrödinger equation (1.2), multiplying $\Phi_J(\mathbf{r};\mathbf{R})^*$ from the left side, and integrating it over electron coordinates $\mathbf{r}$ leads to the following a set of coupled equations of motion of a nuclear wavefunction.

$$\begin{aligned} i\hbar\frac{\partial}{\partial t}X_J(\mathbf{R},t) = \sum_A \sum_I -\frac{\hbar^2}{2M_A}\Big[\left(\nabla_A{}^2\right)_{JI} + 2(\nabla_A)_{JI}\nabla_A + \delta_{JI}\nabla_A{}^2\Big] X_I(\mathbf{R},t) \\ + \sum_I \left(\hat{H}^e(\mathbf{r},\mathbf{R}) + V_{NN}(\mathbf{R})\right)_{JI} X_I(\mathbf{R},t) \end{aligned} \tag{1.6}$$

where

$$(\nabla_A)_{JI} = \langle \Phi_J(\mathbf{r};\mathbf{R}) | \nabla_A | \Phi_I(\mathbf{r};\mathbf{R}) \rangle \tag{1.7 a}$$

$$\left(\nabla_A{}^2\right)_{JI} = \left\langle \Phi_J(\mathbf{r};\mathbf{R}) \middle| \nabla_A{}^2 \middle| \Phi_I(\mathbf{r};\mathbf{R}) \right\rangle \tag{1.7 b}$$

$$\left(\hat{H}^e(\mathbf{r},\mathbf{R}) + \hat{V}_{NN}(\mathbf{R})\right)_{JI} = \left\langle \Phi_J(\mathbf{r};\mathbf{R}) \middle| \hat{H}^e(\mathbf{r},\mathbf{R}) + \hat{V}_{NN}(\mathbf{R}) \middle| \Phi_I(\mathbf{r};\mathbf{R}) \right\rangle \tag{1.7 c}$$

Eq. (1.7 a) and (1.7 b) are the first and second-order non-adiabatic coupling vectors. Now the term in Eq. (1.7 c) is equal to zero except for a diagonal term $I = J$ because eigenfunctions were chosen as the basis. In Eq. (1.6), the motion of Jth nuclear wavefunction could be coupled with every other Ith nuclear wavefunction through non-adiabatic couplings. Under the Born-Oppenheimer approximation [5], Eq. (1.6) is simplified by ignoring non-adiabatic coupling terms of Eq. (1.7 a) and Eq. (1.7 b):

$$i\hbar\frac{\partial}{\partial t}X_J(\mathbf{R},t) = \left[\sum_A -\frac{\hbar^2}{2M_A}{\nabla_A}^2 + E_J^{\mathrm{BO}}(\mathbf{R})\right]X_J(\mathbf{R},t) \tag{1.8}$$

where

$$E_J^{\mathrm{BO}}(\mathbf{R}) = \left(\hat{H}^e(\mathbf{r},\mathbf{R}) + V_{NN}(\mathbf{R})\right)_{JJ} \tag{1.9}$$

Eq. (1.8) no longer contains interaction terms between different electronic states (JI components). This means that the nuclear wavefunction associated with a given adiabatic state will continue to be conserved within that adiabatic electronic state. Hence, non-adiabatic transition refers to the process that causes a nuclear wave packet to move back and forth between or to branch into different adiabatic states. There are several ways to treat the chemical reaction dynamics involving non-adiabatic transitions. A direct way is to solve Eq. (1.2) with full quantum treatment for nuclei and electrons. However, its applicability is very limited, with only a few atomic degrees of freedom. Therefore, various approximate approaches have been explored. Multi configuration time dependent Hartree (MCTDH) [6, 7] is one of the gold standards of the approximated quantum dynamics method, which expands nuclear wavefunctions in terms of single-particle wavefunctions. MCTDH and its extension, multilayer MCTDH [8–10], can handle from a few tens to several hundred nuclear degrees of

freedom, which is significantly large for a quantum dynamics method, On the other hand, one should represent an electronic Hamiltonian operator with analytic forms or perform a global fitting for potential energy surfaces, which is generally difficult if your target system is large and its potential energy surfaces are more complex. In the exact factorization approach [11, 12], the total molecular wavefunction is represented exactly as a single product of the time-dependent nuclear and electronic wavefunctions. MCTDH and the exact factorization approach are highly accurate quantum dynamics methods, but they require potential energy surfaces and interstate couplings for the target preliminary. Then if you use quantum chemical calculations for them, the cost is enormous, limiting nuclear degrees of freedom. Introducing classical treatment of nuclear degrees of freedom allows for a direct or on-the-fly approach that does not require potential energy surfaces and interstate couplings prior to dynamics calculations. The huge advantage of on-the-fly approach is that it can be applied to any system, directly using accurate potential energy surfaces and interstate couplings obtained from quantum chemical calculations for the time evolution of the target system. There are three types of methods for approximating nuclear wavefunctions by multi-dimensional Gaussian functions (trajectory basis functions: TBSs): direct dynamics variational multi-configuration Gaussian (DD-vMCG) [13], Multi-configurational Ehrenfest (MCE) [14, 15], and full/ab initio multiple spawning (FMS [16, 17]/AIMS [18, 19]). TBFs evolve in time, following variational quantum trajectories from the Dirac-Frankel variational principle, mean-field Ehrenfest trajectory in the MCE method, and classical trajectories in FMS/AIMS methods.

Mean-field (Ehrenfest dynamics) [20] and trajectory surface hopping (SH) [21, 22] methods treat nuclear degrees of freedom by the classical equation of motion. In the Ehrenfest method, nuclei move over a mean field average of potential energy surfaces. It is effective in situations where many electronic states are close to each other, but it is difficult to under-

stand the result intuitively. In the TSH method, nuclei move on a single potential energy surface, and non-adiabatic transitions are represented by stochastically switching the potential energy surface on which the nuclei stay in a non-adiabatic region. The first method to treat non-adiabatic transitions in a classical trajectory-based method was proposed by Bjerre and Nikitin [23], in which a trajectory is bifurcated into two based on a Landau-Zener non-adiabatic transition probability estimated at an intersection. Then, the prototype of the SH method was proposed by Tully and Preston in 1971 [21], in which the Landau-Zener non-adiabatic transition probability is compared with a random number to determine whether a transition occurs or not. Later, Tully proposed the "fewest switches" algorithm in 1990 [22]. Now, ab initio molecular dynamics (AIMD) combined with the SH method [24, 25] has become widely used, considering non-adiabatic transitions with all nuclear degrees of freedom.

Non-radiative processes include internal conversion, which is a transition between the same spin states, as well as intersystem crossing, which is a transition between different spin states. Intersystem crossing is a spin-forbidden transition allowed by spin–orbit relativistic effect. It is widely recognized that spin–orbit coupling is important in systems containing heavy elements such as halogen atom (Br or I atom), transition metals and rare-earth elements, but efficient intersystem crossing occurs in systems consisting only of light elements [26]. The latter is threfore also important in photochemistry. As already mentioned, intersystem crossing is caused by spin–orbit coupling, not non-adiabatic coupling, so in this sense, intersystem crossing is not a non-adiabatic transition. Non-adiabatic transition is, in general, used to refer to a transition between adiabatic states. However, it should be mentioned that non-adiabatic dynamics simulation may include both internal conversion and intersystem crossing, since methodologically they are treated in the same framework. Given the electronic Hamiltonian of a molecular system, the adiabatic states are uniquely determined as an eigenstate of the Hamiltonian. In this case, the off-diagonal terms of the

electronic Hamiltonian matrix are zero, and there can be no interaction term between different adiabatic states in an isolated system with no external field other than differential terms of nuclear coordinates, Eq. (1.7 a) and Eq. (1.7 b). On the other hand, diabatic states are defined in such a way that their characters remain constant with respect to the nuclear coordinates, usually keeping the non-adiabatic coupling at zero. In this case, the electron Hamiltonian matrix is no longer diagonal. In short, the interaction between adiabatic states originates from nuclear motions Eq. (1.7 a) and Eq. (1.7 b), whereas the interaction between diabatic states originates from terms in the electronic Hamiltonian. Usually, in quantum chemical calculations, the eigenstates (adiabatic states) of the non-relativistic electronic Hamiltonian can be obtained. Adiabatic and diabatic states can be converted to each other if a transformation matrix is known, but in general, the transformation can not be uniquely determined. In addition, it is generally impossible to define diabatic states so that non-adiabatic coupling between them is zero over any nuclear configuration. Thus, it is not versatile except for some special cases.

However, both diabatic and adiabatic states can be obtained in the case of intersystem crossing. The spin–orbit coupling that causes intersystem crossing is a relativistic effect, which is derived from the Dirac equation [27, 28]. Although relativistic quantum chemistry has made significant progress [29–35], One standard method to take into account the spin–orbit coupling is to perturbatively incorporate relativistic effects into non-relativistic Hamiltonian with the spin–orbit Hamiltonian:

$$\hat{H}^{e'} = \hat{H}^{e} + \hat{H}^{\mathrm{SO}} \tag{1.10}$$

Here we can obtain the eigen (adiabatic) states of each Hamiltonian of Eq. (1.3) and Eq. (1.10). The eigenstates of Eq. (1.3) are no longer eigen (adiabatic) states for Eq. (1.10),

but diabatic states. In this thesis, the eigenstates obtained by using Eq. (1.3) are usually calculated as spin eigenstates and are therefore referred to as spin-pure states. On the other hand, the eigenstates for Eq (1.10) are no longer spin eigenstates, which means the states are mixtures of different spin states and are hence referred to as spin-mixed states. Spin-pure states are also called spin-diabatic states or MCH (molecular Coulomb Hamiltonian) states. Spin-mixed states are also called spin-adiabatic states or diagonal states. Potential energy surfaces of both spin-pure and spin-mixed states can be used in spin-inversion dynamics. A full quantum dynamics simulation should yield the same results with either type of potential energy surface if it is possible. However, in the SH-AIMD method, which treats nuclei classically, the results could differ depending on which potential energy surface is used.

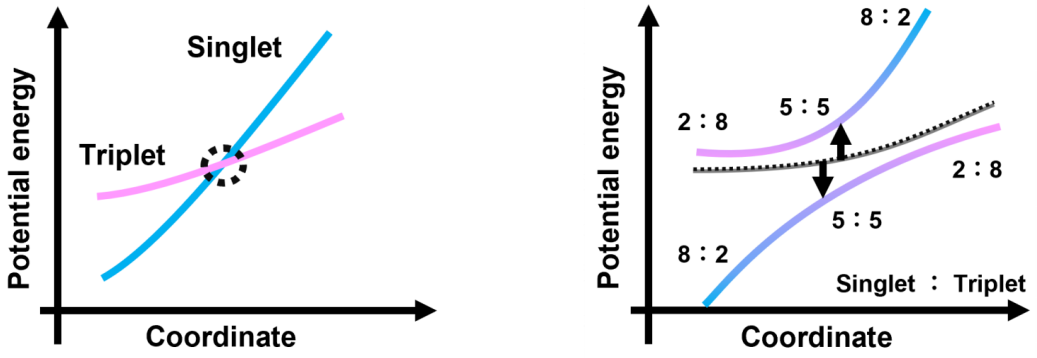

(a) Spin-pure potentials **(b)** Spin-mixed potentials

Figure 1.1. Two types of potential energy surfaces

Proper description of electronic ground and excited states is a top priority in non-adiabatic dynamics. In particular, special methods are required to handle cases where multiple electronic states are close to each other or quasi-degenerate. There are two major frameworks for electronic structure calculations: ab initio wavefunction theory (WFT) and density functional theory (DFT). The Schrödinger equation for electrons cannot be solved analyti-

cally except for hydrogen atoms (many-body problem). Hartree-Fock (HF) method [36, 37] approximates an electronic ground state with a single Slater determinant, and the molecular orbitals (MOs) are determined according to the variational principle. HF method can estimate 99% of the electronic ground state energy, but the remaining 1%, in other words, electron correlation energy is important for chemical accuracy, so the purpose of the WFT known as post-HF methods is to efficiently take into account for the electron correlation energy and improve the wavefunction. Hence, HF today plays an important role as an initial guess for the post-HF methods. In a non-relativistic manner, the electron correlation is defined as the difference between the HF energy and the full configuration interaction (FCI) energy. In the FCI method, the electronic ground and excited states are represented as linear combinations of any configuration, constructed from a set of HF MOs. This simple method gives an exact solution only where an infinite number of basis functions and an infinite number of configurations are available, but in practice, as the number of electrons and basis functions become large, the computation time becomes infeasible within practical limits, enforcing to truncate the basis and configurations. Considering all excitation configurations, the computational cost of FCI is high. In truncated CI methods like CIS (CI with all single excitation configurations), CISD (CI with all single and double excitation configurations), and others, the number of configurations to be considered is reduced, resulting in a feasible computation time. The problem with a truncated CI method is that it is not size-consistent, making it difficult to evaluate an interaction energy. While CI methods involve the correlation energy by incorporating excitation configurations linearly, the coupled-cluster (CC) methods [38] involve it by incorporating excitation configurations non-linearly. The CC method is size-consistent and size-extensive and the CC with all single, double and perturbatively triple excitation configurations (CCSD(T)) [39] is referred to as golden standard. As the CC methods for excited state calculations, the equation-of-motion (EOM-) CC

method [40,41], equivalent to symmetry-adapted cluster (SAC-) CI method [42–44], and CC linear response (LR) method [45, 46] are also known. The many-body perturbation theory (MBPT) method is a method of perturbatively incorporating the electron correlations, and Møller-Plesset perturbation theory method [47] (MP2, MP3, and higher order MP method) is widely used for ground-state calculations. The perturbation theory assumes that the zeroth order wavefunction can describe most of the target system. Therefore, a single Slater determinant, i.e., an HF wavefunction as a zeroth order wavefunction, is not accurate when an excited state is close to the ground state, e.g., when dissociation occurs where the so-called static correlation is important.

Multi-configurational self-consistent field (MCSCF) [48–50] is a method to optimize MO and CI coefficients according to the variational principle, incorporating static correlations absence in the HF method. One of the most important variants of MCSCF is the complete active space self-consistent field (CASSCF). In the CASSCF method, the FCI and SCF procedures are simultaneously performed using all configurations generated from a selected active space which includes electrons and MOs to be important. There are also other variants, restricted active space self-consistent field (RASSCF) [51] which restricts excitation configurations within active space, and general active space self-consistent field (GASSCF) [51], which is a more general form. The drawback of these methods is that the choice of active space is entirely the responsibility of users, so they cannot be used in a black-box fashion, putting off non-expert users. Additionally, when a chemical reaction undergoes multiple steps and important MOs are different for each step, the user needs to add all relevant MOs to the active space, which increases the computational cost. State-averaged (SA-) CASSCF [49, 50] is used to describe the ground and excited states. In the SA-CASSCF procedure, the variational principle is applied to the weighted (usually the same weight for all states) average energy of the ground and excited states, optimizing MO

and CI coefficients of the ground and excited states. Despite the difficulty of selecting the active space, the SA-CASSCF method has the advantage of allowing the consideration of static correlations and treating the ground and excited states on equal footing. A method that uses a single-determinant such as an HF wavefunction as a reference state is called a single-reference method, whereas a method that uses an MCSCF wavefunction as a reference state is called the multi-reference (MR) method. Multi-reference (MR) methods (e.g., MRCI, MRCC, MRMBPT) incorporate dynamical electron correlations, which are absent in the MCSCF, to achieve highly quantitative quantum chemical calculations. The MRCI method considers additional excitation configurations outside the active space in the CASSCF. It is generally more costly than the other MR methods. The MRCC method [52, 53] is more complex in formulation and algorithm than other MR methods, and its implementation is limited [54]. Complete active space second-order perturbation theory (CASPT2) [55, 56], one of the MRMBPT methods, has recently made much progress. Although the CASPT2 method can be applied to excited states in a state-specific manner, it is no longer variational, and in the situation where multiple electronic states are close to each other, quasi-degenerate perturbation theory is required to describe the ground and excited states correctly. Thus, several multi-state variants [57–60] have been developed. As other MRMBPT methods, MRMP [61], multi-configurational quasi-degenerate perturbation theory (MCQDPT) [62] and its multi-state variant [63], n-electron valence state perturbation theory (NEVPT) [64] and its multi-state variant (quasi-degenerate NEVPT) [65], have also been developed.

The DFT method, so-called Kohn-Sham DFT [66–68], has grown to the point that today, it surpasses ab initio methods in the number of uses in scientific research. The DFT, as the name implies, is a method based on electron density, and its foundation, the Hohenberg-Kohn theorem [69, 70], asserts that “electron energy or any physical quantitatively is a unique functional of electron density”. The Hohenberg-Kohn theorem guarantees

that the exact functional of the electron density provides the exact electron energy. However, exact functionals for exchange and correlation are not known [70]. Then, various exchange and correlation functionals with a local density approximation (LDA) [66], a generalized gradient approximation (GGA) [67,68,71], and a semi-empirical [72], or a machine learning technique [73]. Various functionals have been developed for various purposes, and users have difficulty in selecting an appropriate functional to their target system or reactions. Despite its difficulty, the DFT method has been used in many studies because of its inexpensive computational cost comparable to the HF method, but with higher accuracy, and generality that makes it easy to use even for non-experts. The DFT method is also extended to excited state calculations as time-dependent (TD-) DFT [74,75]. The TD-DFT describes the excited states using the ground state obtained from the DFT calculation as the reference state. Therefore, it breaks down around a conical intersection region between the ground state and the lowest excited state. Spin-flip (SF-) TDDFT [76] overcomes the limitation by using a high spin state as a reference state, for example, the lowest triplet state for singlet ground and excited states. However, the spin-flip method suffers from spin-contamination due to its spin incompleteness [77], and it sometimes makes it difficult to perform geometry optimization, reaction path calculation, or molecular dynamics simulation [78,79]. Recently, Lee, Choi, and co-workers have developed the mixed-reference SF-TDDFT (MRSF-TDDFT) [80,81], which avoids spin-contamination by using a mixed-reference reduced density matrix.

Given practical applicability to SH-AIMD simulations, electronic structure methods must be able to efficiently calculate electronic energies where multiple electronic states are close to each other as well as their gradients, non-adiabatic coupling, and spin–orbit couplings. The SA-CASSCF method has long been used since the beginning of the SH-AIMD study because it is superior in terms of a well-balanced description for electronic ground and excited states and availability to compute non-adiabatic coupling vectors analytically.

There are an increasing number of methods that can compute NAC vectors analytically. In particular, the CASPT2 method, combined with the density fitting technique, provides fast computations of analytic derivatives and has been applied to SH-AIMD simulations [82]. In the DFT framework, MRSF-TDDFT which overcomes the limitations of TDDFT and SF-TDDFT has been developed and also applied to SH-AIMD simulations [83–85]. To compute spin–orbit coupling, SA-CASSCF or MRCI is mainly used. Some software and third-party programs in recent development can compute spin–orbit coupling at the TDDFT level. Thus, we have more options for calculating SOC than before. One trend in calculating electronic structure-based quantitie such as potential energy, its gradient, and interstate couplings is to predict them using machine learning/deep learning techniques. In SH-AIMD simulations, a large number of quantum chemical calculations are performed for each independent classical trajectory in an on-the-fly manner. However, all independent classical trajectories do not travel in completely different regions but rather run in somewhat the same or neighboring regions. thus, efficiently sampling the structure and learning potential surfaces and other quantities can lead to significant resource savings. Attempts for excited states have been limited, but there have been some successes.

The applicability of the SH-AIMD method has increased in recent years with the development of quantum chemical methods and the advent of machine-learning techniques, which play an important role in describing non-adiabatic dynamics via internal conversion and intersystem crossing. As mentioned before, there are two types of potential energy surfaces that can be utilized for SH-AIMD simulations of intersystem crossing dynamics, but the dependence of the SH-AIMD method on the type of potential energy surface has never quantitatively been discussed in terms of spin–orbit coupling strengths yet. This thesis consists of the following five chapters. **Chapter 1** is a general introduction. In **Chapter 2**, the dependency of SH-AIMD method on spin-pure (spin-diabatic) and spin-mixed (spin-

adiabatic) potential energy surfaces was investigated using Tully's fewest switches (TFS) algorithm. In **Chapter 3**, a SH-AIMD code with Zhu-Nakamura (ZN) global switching algorithm is developed. The code is applied to same systems in **Chapter 2** and the result is compared to that of the TFS algorithm. In **Chapter 4**, excited-state intramolecular proton transfer and subsequent dynamics of *ortho*-nitrophenol are investigated based on nonadiabatic molecular dynamics using the SH-AIMD code develped in **Chapter 3**. **Chapter 5** summarizes this thesis and describes future perspectives.

Chapter II

Intersystem crossing dynamics based on spin-pure and spin-mixed potential energy surfaces with Tully's fewest switches algorithm

Abstract

Surface hopping ab initio molecular dynamics (SH-AIMD) simulations based on spin-pure and spin-mixed states are performed for a series of XH_2 (X = Si, Ge, Sn, Pb) molecules, which have different spin-orbit coupling (SOC) strengths.

2.1 Introduction

Ab initio molecular dynamics (AIMD) is a classical trajectory method that traces the time evolution of nuclear motion using the nuclear force determined on the fly from ab initio electronic structure calculations [24, 25]. The AIMD was extended with the surface hopping (SH) method, the widely used Tully's fewest switches (TFS) algorithm [22], to describe photochemical reactions proceeding in excited states with non-adiabatic transitions between electronic adiabatic states [86, 87]. The method has been applied to discussions of excited state lifetime and dynamic reaction pathways in photoisomerization reactions [88], and solvent effects on non-adiabatic transitions of photoreactions in solution by a hybrid quantum mechanics and molecular mechanics framework [89, 90]. These applications focused on the non-adiabatic transition between electronic states of the same spin-symmetry, termed internal conversion (IC), induced by non-adiabatic coupling (NAC). The NAC term is used in SH-AIMD simulations based on the TFS algorithm (TFS-SH-AIMD) to solve the time-dependent Schrödinger equation for the electronic amplitude. In the early stages of the TFS-SH-AIMD method, the NAC term, a matrix element of the nuclear coordinate derivative calculated analytically at the state-averaged complete active space self-consistent field (SA-CASSCF) level, was used [49, 50]. In recent applications, however, instead of calculating the NAC term, a scheme that numerically calculates the matrix elements of the time derivative with the electronic wavefunction at two geometries along the trajectory has also been used [91, 92]. Nowadays, the NAC term can also be computed analytically by several sophisticated methods [60, 93–96] and is employed in some applications to IC dynamics in TFS-SH-AIMD simulations [82, 95, 97–99].

Recent theoretical developments have brought attention to the state transition between

different spin-symmetry states, termed intersystem crossing (ISC), induced by spin–orbit coupling (SOC). It is well known that the SOC is important in a system with a heavy element because each spin-pure (spin-diabatic) state is individually meaningless, and the spin-mixed (spin-adiabatic) state, a mixture of spin-pure states, is dominant. Namely, for molecular systems containing elements located in period 4 or later of the periodic table, the discussion should be based on spin-mixed states. To perform such SH-AIMD simulations based on spin-mixed states, the SOC must be taken into account for the potential gradient and the NAC. Unfortunately, there are only a few methods and programs that can analytically calculate the gradient and NAC terms of the spin-mixed states [100–102], and their application to ISC dynamics has not yet progressed. As one alternative solution, Kamiya *et al.* [103] developed a TFS-SH-AIMD code utilizing numerically evaluated gradients and NAC terms of the spin-mixed states and applied it to the photodissociation reaction of methyl iodide. As another solution, Mai *et al.* developed a TFS-SH-AIMD method named SHARC [104, 105] with approximated gradients and NAC terms of the spin-mixed states. Their approximate derivatives do not include the derivative of the SOC term, but avoiding numerical differentiation allows TFS-SH-AIMD simulations based on spin-mixed states to be performed at reasonable computational costs. The development of these computational methods is important not only for systems with large SOCs but also for those with small SOCs. As El-Sayed first pointed out, ultrafast ISC of light-element molecules can occur even with small SOC [26], which has also been demonstrated in theoretical studies using SHARC [106, 107]. This reminds us that SOCs play an essential role in photochemical reactions, regardless of their size, and the SH-AIMD method is expected to make a significant contribution to the elucidation of such ISC processes in the future.

In studying the process of ISC by SH-AIMD simulations, there are two choices of potential energy surface (PES): one in the spin-pure state and the other in the spin-mixed

state. For systems with small SOC, the difference between the two PESs is not so large that it is efficient to use the spin-pure state PESs from a computational cost viewpoint, and SOC is only considered when evaluating SH probabilities [108–111]. However, for systems with large SOC, it is necessary to use the spin-mixed PESs even in the time evolution of the nuclei; SOC affects the nuclear motion via the potential energy gradient and the NAC term. Granucci *et al.* [112] performed TFS-based trajectory surface hopping simulations based on both types of PESs using a model with a large SOC ($\sim$ 310 cm-1) and compared them with quantum dynamics results, concluding that the use of spin-mixed PESs provides more accurate results. Peng *et al.* [113] investigated the accuracy of the TFS-based trajectory surface hopping method for intersystem crossing dynamics based on modified linear vibronic coupling of rhenium(I) tricarbonyl complex by comparing the results of quantum dynamics simulations using the multiconfigurational time-dependent Hartree (MCTDH) method. They also compared the time evolution of the spin-adiabatic electronic populations obtained from three different models with fixed SOC. However, no systematic study has yet been reported on how the dynamics based on spin-pure and spin-mixed surfaces deviate depending on SOC strength in real molecular systems.

Recently, there has been a gradual increase in the number of studies performing SH-AIMD calculations for the intersystem crossing problems [103, 106–111], To discuss the applicability of the SH-AIMD method to excited-state reactions with intersystem crossings in molecular systems, we perform spin-pure and spin-mixed PES-based SH-AIMD simulations for group 14 element dihydrides MH_2 (M = Si, Ge, Sn, Pb) with different SOC strength.

2.2 Tully's fewest switches algorithm

In this section, Tully's fewest switches (TFS) algorithm is briefly introduced. First, the time-dependent electronic wavefunction is expanded in terms of time-independent electronic basis $\{\Phi^e(\mathbf{r};\mathbf{R})\}_I$ as follows.

$$\Psi(\mathbf{r},\mathbf{R}(t)) = \sum_I C_I(t)\,\Phi_I^e(\mathbf{r};\mathbf{R}(t)) \tag{2.2.1}$$

To obtain the time evolution of the electronic wavefunction, Eq. (2.2.1) is inserted into the electronic time-dependent Schrödinger equation,

$$i\hbar\frac{\partial}{\partial t}\Psi(\mathbf{r},\mathbf{R}(t)) = \hat{H}^e\Psi(\mathbf{r},\mathbf{R}(t)) \tag{2.2.2}$$

where H^e is the electronic Hamiltonian which can include the spin-orbit coupling or the laser field term in addition to the Coulomb terms, and then, by multiplying $\Phi_J^{e*}(\mathbf{r};\mathbf{R})$ from the left and integrating over $\mathbf{r}$, the following time-evolution equation for the electronic amplitude $C_J(t)$ is given by

$$i\hbar\frac{\partial}{\partial t}C_J(t) = \sum_I C_I(t)\left(V_{JI}(\mathbf{R}) - i\hbar\mathcal{T}_{JI}\right) \tag{2.2.3 a}$$

$$= \sum_I C_I(t)\left(V_{JI}(\mathbf{R}) - i\hbar\dot{\mathbf{R}}\cdot\mathbf{d}_{JI}(\mathbf{R})\right) \tag{2.2.3 b}$$

$V_{IJ}(\mathbf{R})$ is a matrix element of the electronic Hamiltonian (H^e) on the basis of electronic basis $\{\Phi^e(\mathbf{r};\mathbf{R})\}_I$ as follows.

$$V_{IJ}(\mathbf{R}) = \left\langle \Phi_I^e(\mathbf{r};\mathbf{R}) \middle| \hat{H}^e \middle| \Phi_J^e(\mathbf{r};\mathbf{R}) \right\rangle \tag{2.2.4}$$

$\mathcal{T}_{JI}$ is a matrix element of time-differentiation term, $\left\langle \Phi_J^e(\mathbf{r};\mathbf{R}) \middle| \partial/\partial t \middle| \Phi_I^e(\mathbf{r};\mathbf{R}) \right\rangle$, which can be transformed to the dot product of the nuclear velocity vector, $\dot{\mathbf{R}}$ and the non-adiabatic coupling vector, $\mathbf{d}_{JI}(\mathbf{R})$.

$$\mathcal{T}_{JI} = \left\langle \Phi_J^e(\mathbf{r};\mathbf{R}) \middle| \frac{\partial}{\partial t} \middle| \Phi_I^e(\mathbf{r};\mathbf{R}) \right\rangle \tag{2.2.5 a}$$

$$= \left\langle \Phi_J^e(\mathbf{r};\mathbf{R}) \middle| \frac{\partial \mathbf{R}}{\partial t} \cdot \frac{\partial}{\partial \mathbf{R}} \middle| \Phi_I^e(\mathbf{r};\mathbf{R}) \right\rangle$$

$$= \frac{\partial \mathbf{R}}{\partial t} \cdot \left\langle \Phi_J^e(\mathbf{r};\mathbf{R}) \middle| \frac{\partial}{\partial \mathbf{R}} \middle| \Phi_I^e(\mathbf{r};\mathbf{R}) \right\rangle$$

$$= \dot{\mathbf{R}} \cdot \mathbf{d}_{JI}(\mathbf{R}) \tag{2.2.5 b}$$

Historically, Eq. (2.2.5 b) has been widely used in studies using the TFS algorithm and algorithms and programs that can compute a non-adiabatic coupling vector have been developed acoordingly [60, 93–96]. However, recently the numerical evaluation of Eq. (2.2.5 a) that computes an overlap of wavefunctions at two geometries along a classical trajectory is also preferred as a simpler method for electronic structure methods where a non-adiabatic coupling vector is not available [91, 92].

In the framework of the SH method, the electronic wavefunction, $\Psi(\mathbf{r}, \mathbf{R}(t))$ is repre-

sented as a linear combination of all coupled electronic states, whereas nuclear coordinates are propagated according to the gradient of a potential energy surface of a single electronic basis. To describe non-adiabatic transitions, the electronic state where nuclei stay is stochastically switched from one to another using the hopping probability which is based on the time evolution of the electronic wavefunction.

$$g_{IJ}(t) = \frac{2\hbar^{-1}\,\mathrm{Im}\left[\left\{C_J(t)\,C_I^*(t)\right\}^* V_{JI}(\mathbf{R}(t))\right] - 2\,\mathrm{Re}\left[\left\{C_J(t)\,C_I^*(t)\right\}^* \dot{\mathbf{R}}\cdot\mathbf{d}_{JI}(\mathbf{R}(t))\right]}{C_I(t)\,C_I^*(t)}\Delta t \quad (2.2.6)$$

After the switching, the atomic velocities are scaled in the NAC vector direction to conserve total energy.

2.3 Results and Discussions

In order to investigate the influences of differences between spin-pure and spin-mixed potential energy surfaces on SH-AIMD simulations, dihydride molecules of 14 group elements: MH_2 (M = Si, Ge, Sn, Pb) except for CH_2 were chosen as target molecules. The SOC of MH_2 increases with the period of the M atom. Potential energy surfaces of spin-pure and spin-mixed states of MH_2 and CH_2 were investigated by Matsunaga *et al.* in 1996 [114]. According to their study, CH_2 is unique as follows. The ground state of MH_2 (M = Si, Ge, Sn, Pb) is a singlet state, whereas that of CH_2 is a triplet state, and singlet-triplet crossing is located away from the equilibrium structure in the MH_2 case, but located near the singlet equilibrium structure in the CH_2 case. Considering the order of electronic states and crossing positions, MH_2 systems represent general intersystem crossing than CH_2 and are appropriate as targets of this study. However, the special CH_2 case is interesting and should be examined in another study.

Electronic structure calculation SA-CASSCF calculations with the active space (6e, 6o) were performed to obtain the singlet (S_0) and triplet (T_1) spin-pure potential energies of the group 14 dihydride MH_2 (M = Si, Ge, Sn, Pb). Based on the SA-CASSCF wave functions, SOC matrix elements [115] were calculated using the Breit-Pauli operator for SiH_2 and SO pseudopotentials for GeH_2, SnH_2, and PbH_2. Then, spin-mixed potential energies were obtained by diagonalizing the SOC matrix. The cc-pVDZ basis sets were used for H and Si, [116, 117] and the cc-pVDZ-PP basis sets for Ge, Sn, and Pb [118]. All electronic structure calculations were carried out using Molpro2012.1 [119, 120].

2.3.1 Geometries of equilibrium structure and MESX structure

Geometry optimization using numerical gradients by central difference scheme with a step of 0.005 Bohr were employed using GRRM17 [121, 122]. **Table 2.1** shows geometrical parameters, the H–M bond length and the H–M–H bond angle, for minima on the spin-pure PESs ($S_{0\text{-min}}$, $T_{1\text{-min}}$) and minimum on the seam of crossing (MESX) between S_0 and T_1 PESs for the dihydride MH_2 (M = Si, Ge, Sn, Pb). Every strucutre is in C_{2v} symmetry. The minima of S_0 and T_1 states are characterized by the H–M–H bond angle: about 92°for $S_{0\text{-min}}$ and 118°for $T_{1\text{-min}}$. For MESX, the H–M–H bond angle is ranged from 126 to 145°. The SOC between S_0 and T_1 states at MESX was calculated to be 54.66, 384.17, 918.05, and 3152.55 cm^{-1} for SiH_2, GeH_2, SnH_2, and PbH_2, respectively. **Table 2.1** also shows geometrical parameters for minima on the spin-mixed PESs (1^{st}_{min}, 4^{th}_{min}), which correspond to $S_{0\text{-min}}$ and $T_{1\text{-min}}$, respectively. For PbH_2 with the largest SOC, the difference in the bond angle is not so small. Those results are in good agreement with those reported by Matsunaga*et al.* [114].

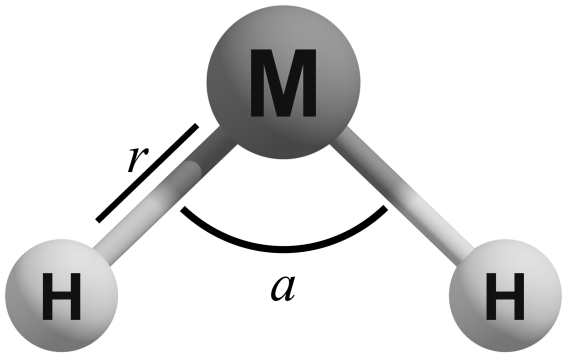

Figure 2.1. MH_2 molecule

Table 2.1. H–M bond length (r in Å) and H–M–H bond angle (a in degrees) at minima on each PES ($S_{0\text{-min}}$, $T_{1\text{-min}}$, 1^{st}_{min}, and 4^{th}_{min}) and MESX between S_0 and T_1 PESs.

	spin-pure states						spin-mixed states			
	$S_{0\text{-min}}$		$T_{1\text{-min}}$		MESX		1^{st}_{min}		4^{th}_{min}	
M	r	a	r	a	r	a	r	a	r	a
Si	1.554	93.3	1.510	117.8	1.498	126.5	1.554	93.3	1.510	117.7
Ge	1.620	92.3	1.559	118.8	1.537	131.7	1.620	92.3	1.560	118.5
Sn	1.805	91.9	1.743	117.8	1.710	135.2	1.804	92.1	1.746	116.5
Pb	1.887	90.9	1.815	119.9	1.744	145.3	1.882	91.9	1.830	116.0

2.3.2 Potential energy curves for spin-pure and spin-mixed states

Figure 2.2 a shows the potential energy curves (PECs) of the S_0 and the T_1 states and their SOC curves as a function of the H–M–H bond angle with the H–M bond length fixed at $S_{0\text{-min}}$. They show the Landau-Zener type of potential energy crossing in this one-dimensional picture. The SOC is nearly constant around the stable structure but decreases rapidly to zero in the region where the HMH bond angle is close to 180°(linear geometry) due to symmetry requirements, and is delocalized not only in the crossing region but also in a wide range. **Figure 2.2 b** shows the PECs of the lowest (1^{st}) and highest (4^{th}) spin-mixed states. The SOC induces avoided crossing features in the PECs. That is apparent for SnH_2 and PbH_2, especially in the region where two potential energies are energetically close to each other (non-adiabatic region). At the MESX in the spin-pure states, the energy gap between two spin-mixed states was calculated to be 0.014, 0.095, 0.228, and 0.782 eV for SiH_2, GeH_2, SnH_2, and PbH_2, respectively. The spin-pure and spin-mixed PESs could differ significantly in the seam of crossing regions if a molecular system has a large SOC, e.g., 900 cm^{-1} for SnH_2 and 3000 cm^{-1} for PbH_2. Contour plots of potential energy surfaces are also shown in **Fig. 2.3**. The potential energy surfaces are smooth in the plotted range.

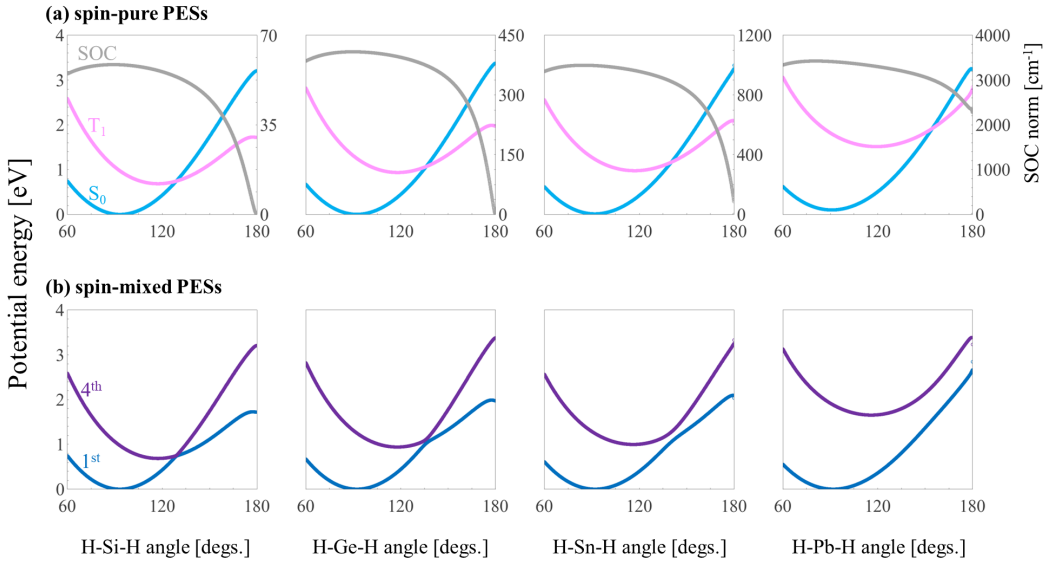

Figure 2.2. Potential energy and SOC curves as a function of the HMH bond angle: (a) S_0 and T_1 spin-pure states and their SOC; (b) 1^{st} and 4^{th} spin-mixed states. The potential energy values are given relative to the value at the 1^{st}_{min} state.

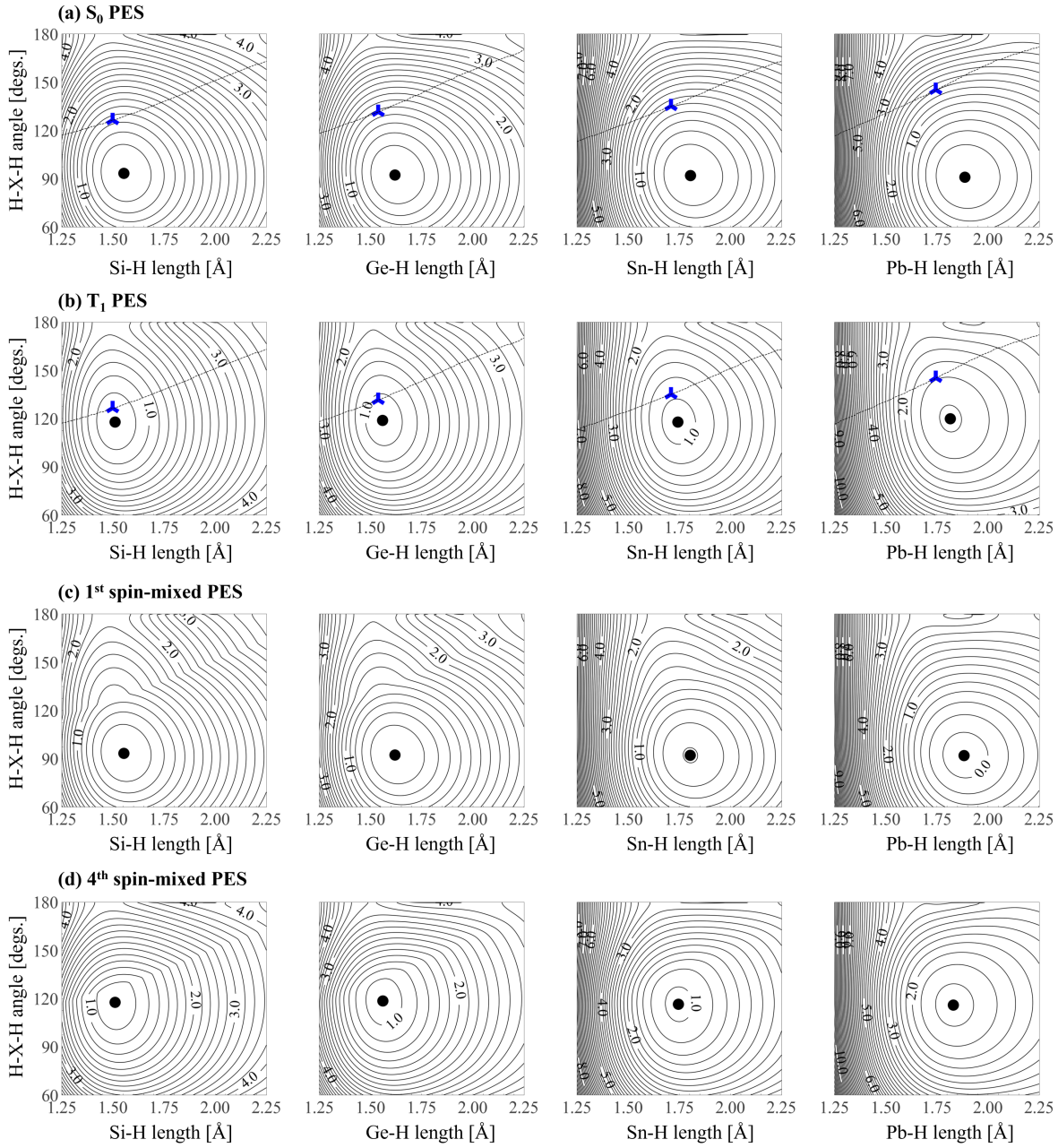

Figure 2.3. Contour plots of potential energy surfaces as a function of the HMH bond angle and HM bond length: (a) S_0 and (b) T_1 spin-pure state and (c) 1^{st} and (d) 4^{th} spin-mixed states. The potential energy values are given relative to the value at the 1^{st}_{min} state. The black dot: an equilibrium structure on each surface. The black dashed line: seam of crossing between S_0 and T_1 states, The blue cross mark: MESX between S_0 and T_1 states,

2.3.3 Spin-orbit coupling and non-adiabatic coupling

Figure 2.4 shows contour plots of (a) the SOC between S_0 and T_1 spin-pure states and (b) the NAC term between 1st and 4th spin-mixed states with respect to the H–M–H bond angle, computed on a two-dimensional coordinate space grid with H–M bond length and H–M–H bond angle. The SOC is delocalized regardless of the seam of crossing (black solid line) because it depends on the character of the electronic states, not on the energy difference. In all cases, the SOC decreases sharply toward regions with a large bond angle and short bond length due to the symmetry requirements. The nonlocality of the SOC affects the accuracy of TFS-SH-AIMD simulations, as discussed in previous studies [112, 113]. The NAC term $d_{\alpha\beta}$ between the αth and βth spin-mixed states with respect to the H–M–H bond angle θ was calculated numerically according to the following formula obtained using polar coordinates,

$$d_{\alpha\beta} = \frac{1}{E_\beta - E_\alpha} \sum_{\mu,\nu} (\mathbf{U}^\dagger)_{\alpha\mu} \left(\frac{1}{r} \left[\frac{1}{\cos\theta} - \frac{1}{\sin\theta} \right] \frac{\partial}{\partial\theta} \mathbf{H}^{\mathrm{SO}} \right)_{\mu\nu} (\mathbf{U})_{\nu\beta} \tag{2.3.1}$$

where **U** denotes a spin-pure to spin-mixed state transformation matrix. Now, only one singlet and one triplet state are considered, but in general, when considering multiple singlet and/or multiple triplet states, NACs between the same spin states should also be considered, refer to the ref [103] for the full formula. As shown in **Fig. 2.4 b**, the NAC is essentially localized near the seam of crossing where the two states are energetically close. However, the localization of NAC around the seam of crossing becomes weaker depending on the strength of SOC. In the case of PbH_2, the maximum of NAC is located in the region of large bond angle and small bond length (upper left region), which is due to the large SOC gradient on the same order as the energy difference between the two spin-mixed states.

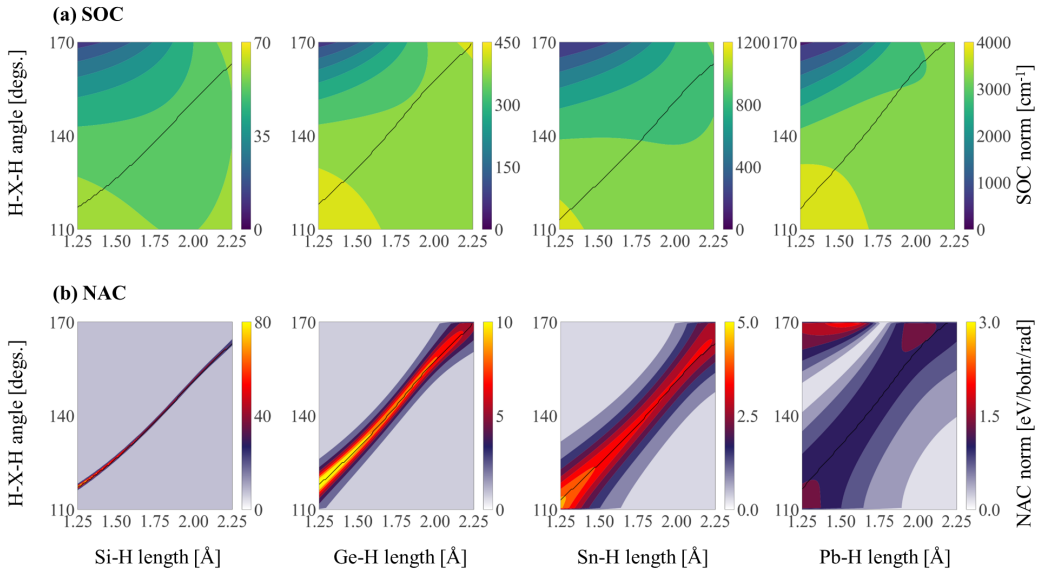

Figure 2.4. Contour plots of (a) the SOC between S_0 and T_1 spin-pure states and (b) the NAC between 1st and 4th spin-mixed states with respect to the H–M–H bond angle on a two-dimensional coordinate space grid with H–M bond length and H–M–H bond angle. A black solid line indicates a seam of crossing between spin-pure S_0 and T_1 PESs.

2.3.4 Tully's fewest switches (TFS)-SH-AIMD simulations using spin-pure/spin-mixed states

All spin-pure and spin-mixed PES-based TFS-SH-AIMD simulations were performed using the SHARC program suite [104, 105]. In simulations of this study, the time-dependent electronic wavefunction (Eq. 2.2.1) is defined by a linear combination of four spin-pure states (S_0 and three sublevels of T_1 state) in spin-pure PES-based simulations, and four spin-mixed states in spin-mixed PES-based simulations. The energy gradient of the spin- state is approximated by a linear combination of energy gradients and non-adiabatic coupling of spin-pure states where the derivative of the SOC term is neglected.

2.3.4.1 Time evolution of electronic wavefunction along trajectories

In TFS-SH-AIMD simulations, nuclei move with state transitions on a single spin-pure or spin-mixed state PESs, while the electronic wavefunction evolves according to the time-dependent Schrödinger equation. **Figure 2.5** shows a typical example of the time evolution of the square of the electronic amplitude (= electronic population) of the triplet state (calculated as the sum of the sub-levels of the T_1 state) along a certain trajectory. The time evolution of the electronic state in which the nuclei stay is indicated by the color of the population curve (T_1: red, S_0: blue). In the case of SiH_2 (SOC $\sim$ 60 cm^{-1}), the time evolution of the electronic population from spin-pure and spin-mixed PES-based simulations is the same for almost all trajectories. The nuclear motion basically follows the electronic state determined stochastically from the electronic population. In the case of GeH_2 (SOC $\sim$ 380 cm^{-1}), the electronic population decreases with time, and small oscillations in the electronic population are observed along with the overall decrease, while in the spin-pure simulation,

the population increases again, showing a different behavior from the spin-mixed simulation. In the case of large SOC SnH_2 (SOC ~ 900 cm^{-1}) and the PbH_2 (SOC ~ 3000 cm^{-1}), the time evolution of the electronic population is quite different between the spin-pure and spin-mixed PES-based simulations, indicating that the spin-pure PES-based simulations do not work well except for SiH_2.

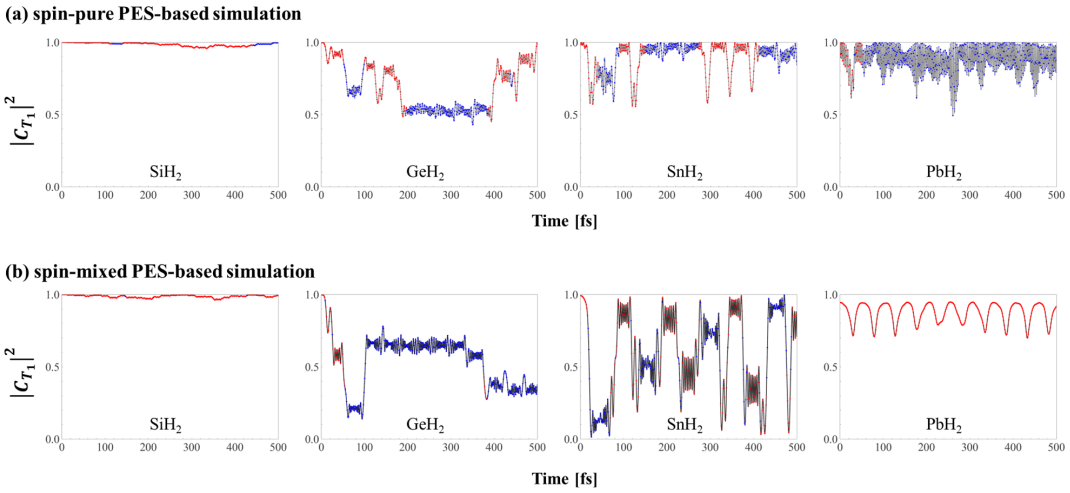

Figure 2.5. A typical example of the time evolution of electronic populations for the T_1 state in each molecular system, obtained from a given trajectory on (a) spin-pure PESs and (b) spin-mixed PESs. Blue indicates that the trajectory stays on the singlet PES and red indicates that the trajectory stays on the triplet PES (assigned to the spin state with greater weight in the spin-mixed state).

2.3.4.2 Time evolution of the fraction of the triplet state of trajectories

Figure 2.6 shows the time evolution of the fraction of T_1 state (denoted by $F_3(t)$) of the trajectories where the nuclei stay in the T_1 state. [123] In order to compare the behavior of the spin-pure and spin-mixed PES-based simulations, we evaluated F_3 (t) for the spin-mixed simulation by considering the contribution of the T_1 component of the spin-mixed states along the trajectories. The fraction of T_1 state (gray dashed line for the spin-pure PES-based simulation and black solid line for the spin-mixed PES-based simulation) decreases over time, except for PbH_2 in the spin-mixed PES-based simulation. First, notice that for PbH_2 there is a clear difference between the spin-pure and spin-mixed PES-based simulations. In the spin-pure simulation of PbH_2, half of the trajectories (73/150) hop to the singlet ground state followed by the dissociation channel, H_2 + Pb. This surface hopping occurs with a large energy difference between the T_1 and S_0 states, which can be understood from the large SOC of PbH_2. However, it is clear that this behavior is not physically correct, indicating that the spin-pure method should not be used for TFS-SH-AIMD simulations of species with large SOCs such as Pb.

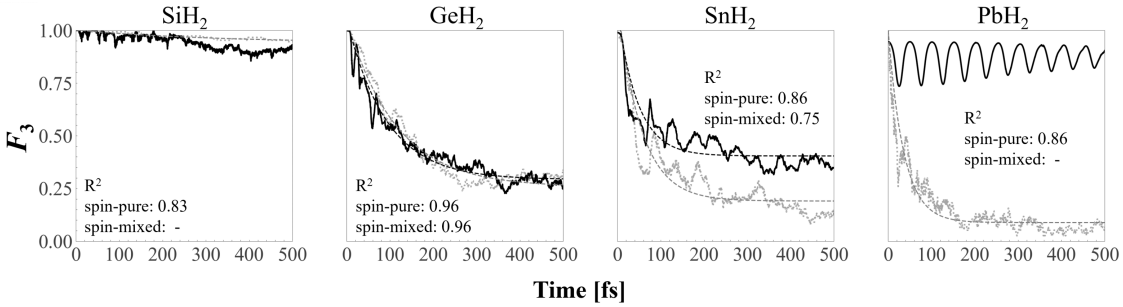

Figure 2.6. Time evolution of the fraction of trajectories staying in the T_1 state calculated from trajectory ensemble based on the spin-pure PESs (dotted gray line) and the spin-mixed PESs (solid black line), calculated from TFS-SH-AIMD simulations. In the spin-mixed PESs, $F_3(t)$ is evaluated considering the contribution of T_1 components in the spin-mixed states. A dashed line represents the fitting regression curve of each $F_3(t)$. R^2 values for each simulation (spin-pure, spin-mixed) are as follows: SiH_2: (0.83, none), GeH_2: (0.96, 0.95), SnH_2: (0.86, 0.75), and PbH_2: (0.86, none).

To quantitatively discuss the $F_3(t)$ decay, the kinetic analysis of each $F_3(t)$ was performed according to previous studies by Varganov *et al.* [123, 124].

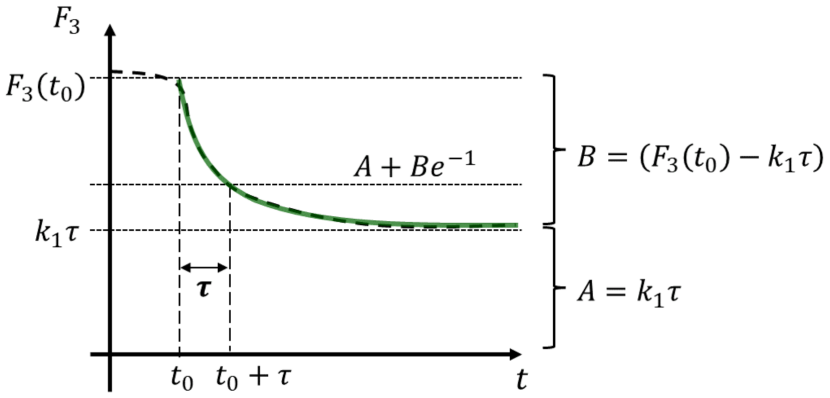

Figure 2.7. Schematic picture of $F_3(t)$ (dashed black line) and parameters used in kinetic analysis. For $F_3(t)$, a region of t t_0 (denoted by green color) was used for the fitting in kinetic analysis.

The rate constants k_1 and k_3 correspond to the ISC processes from S_0 to T_1 and T_1 to

S_0, respectively, and τ represents the lifetime of the T_1 state. The value of τ was evaluated using first-order kinetics based on the following equation [123, 124].

$$F_3(t) = \left[F_3(t_0) - k_1\tau\right] \exp\left(-\frac{t - t_0}{\tau}\right) + k_1\tau \tag{2.3.2}$$
$$\tau = \frac{1}{k_1 + k_3}$$

The results of the kinetic analysis can be found in **Table 2.2**.

Table 2.2. Parameters obtained from kinetic analysis for T_1 fraction decay

	SiH_2		GeH_2		SnH_2		PbH_2	
	spin-pure	spin-mixed	spin-pure	spin-mixed	spin-pure	spin-mixed	spin-pure	spin-mixed
τ / fs	335	–	113	92.1	54.6	46.6	36.1	–
k_1 / 10^{12} s^{-1}	2.81	–	2.26	3.17	3.48	8.67	2.44	–
k_3 / 10^{12} s^{-1}	0.182	–	6.53	7.68	14.8	12.8	2.53	–
$F_3(t_0)$	1.00	–	0.993	0.985	0.933	0.918	1.00	–

For SiH_2, the lifetimes and rate constants (τ, k_1, k_3) were (335 fs, 2.81×10^{12} s^{-1}, 0.182×10^{12} s^{-1}) in the spin-pure PES-based simulation. Zaari *et al.* [123] performed TFS-SH-AIMD simulations with spin-pure PESs for SiH_2 and obtained twice longer lifetimes and one-tenth rate constants (781 fs, 5.2×10^{11} s^{-1}, 7.6×10^{11} s^{-1}). The difference between their results and ours comes from the initial conditions: their initial conditions are generated based on the zero-point energy at $T_{1\text{-min}}$, whereas our initial conditions are generated based on the Wigner distribution of the vibrational ground state at $S_{0\text{-min}}$. In the spin-mixed PES-based simulations, the exponential fit fails due to slight fluctuations in $F_3(t)$, but similar values are expected from the similar behavior of $F_3(t)$.

Fedorov *et al.* [124] performed ab initio multiple spawning (AIMS) simulation for GeH_2 using spin-pure PESs and obtained lifetime and rate constants of (119 fs, 3.1×10^{12} s^{-1}, 5.3×10^{12} s^{-1}), which are similar to our TFS-SH-AIMD simulations with spin-pure PESs (113 fs, 2.26×10^{12} s^{-1}, 6.53×10^{12} s^{-1}). As shown in **Fig. 2.6**, the time evolution of the fraction in the spin-mixed PES-based simulation is similar to that of spin-pure PES-based simulation as well as the lifetimes and rate constants (92.1 fs, 3.17×10^{12} s^{-1}, 7.68×10^{12} s^{-1}) obtained from the spin-mixed PES-based simulation are similar to those of the spin-pure PES-based simulation.

In the case of SnH_2, the lifetimes are relatively similar in the spin-pure and spin-mixed PES-based simulations, 54.6 fs and 46.6 fs, respectively, but the decay rate at 500 fs is overestimated in the former simulation. The similarity in the lifetimes may be due to the similar behavior of the decay in the first 60 fs, but the subsequent decay behavior is not reproduced in the spin-pure simulation. This is evident in k_1 and k_3, where k_1 for the spin-pure simulation (3.48×10^{12} s^{-1}) is less than half the value of the spin-mixed simulation (8.67×10^{12} s^{-1}), while k_3 shows very similar values (14.8×10^{12} s^{-1}, 12.8×10^{12} s^{-1}). This indicates that the ISC from S_0 to T_1 in the spin-pure PES-based simulation is slower than in the spin-mixed PES-based simulation.

In the spin-pure PES-based simulation for PbH_2 (SOC $\sim$ 3000 cm^{-1}), $F_3(t)$ shown in **Fig. 2.6** just decays fast. This rapid decay can be attributed to a large amount of unphysical hopping due to a heavily delocalized SOC at geometries with large energy differences, leading to a conclusion that spin-pure PES-based simulations are not meaningful for PbH_2. This result is consistent with the results of TFS-based trajectory surface hopping simulations for a linear vibronic coupling model (SOC $\sim$ 600 cm^{-1}) by Peng *et al.* [113] In the spin-mixed PES-based simulation, oscillations in $F_3(t)$ are observed, which clearly show a different time propagation than in the spin-pure PES-based simulation, making fitting to Eq. (7) impossi-

ble. In addition, the trajectories stay in the upper spin-mixed state, indicating that there is little surface hopping.

2.3.4.3 Distribution of the number of surface hopping against energy difference

Finally, we discuss the energy difference and frequency of surface hopping when it occurs in spin-pure and spin-mixed PES-based simulations. **Figure 2.8** shows the distribution of surface hopping versus energy difference in the TFS-based simulations. This figure also shows the frequency of surface hopping: in spin-pure simulation, the change from T_1 to S_0 (or vice versa) is counted as surface hopping, whereas in spin-mixed PES-based simulations, surface hopping between spin-mixed states is counted. In the spin-pure PES-based simulation (**Fig. 2.8 a**), the surface hopping occurred at points away from the crossing seam, with large energy differences. This is due to the fact that the SOC is widely delocalized, as shown in **Fig. 2.4 a**, which allows for a wide range of hopping in the TFS-based simulations. In contrast, in the spin-mixed PES-based simulation (**Fig. 2.8 b**), surface hopping occurred where the two spin-mixed states were energetically close together. This is because the NACs are localized in energetically close regions, unlike the spin-pure PES-based ones. As the SOC becomes larger, the energy difference increases to avoid crossing, making surface hopping less likely, and the trajectories stay in the upper state (the values are small in the case of PbH_2 in **Fig. 2.8 b**).

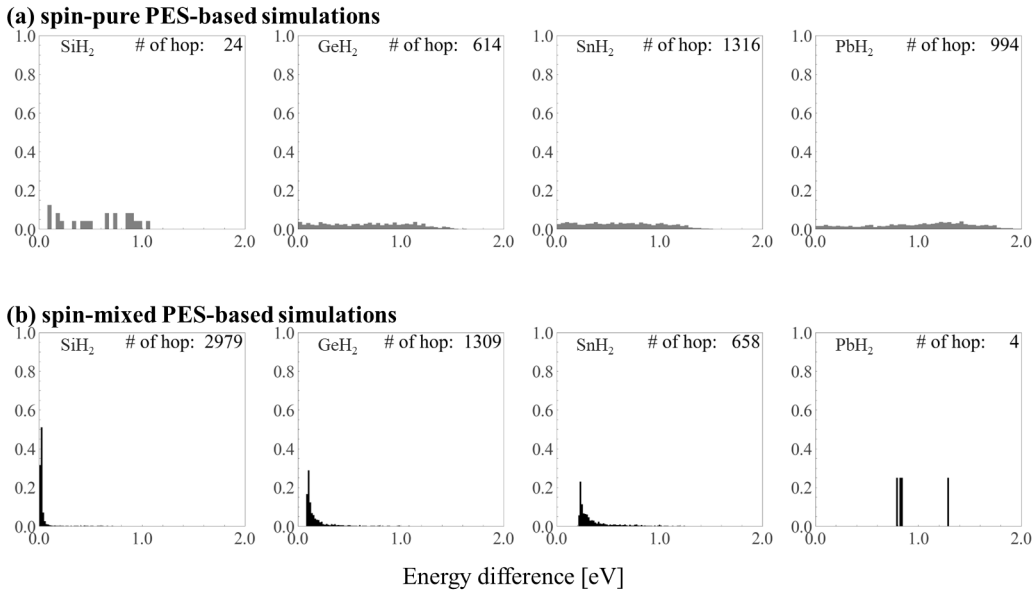

Figure 2.8. The distribution of energy differences between states when surface hopping occurs in simulations using the TFS algorithm, for (A) spin-pure PES-based simulations and (B) spin-mixed PES-based simulations

2.4 Conclusion

In recent years, SH-AIMD calculations for chemical reactions involving excited states, such as photochemical reactions, have been carried out to discuss reaction mechanisms at the atomic level that cannot be clarified by experiments alone. First, theoretical development and application studies of internal conversion between the same spin states preceded, followed by theoretical development and application studies of intersystem crossing between different spin states. In the case of intersystem crossing, unlike internal conversion, a result of SH-AIMD simulation depends on whether spin-pure or spin-mixed states are used. Since the SOC governing intersystem crossing becomes larger for elements lower on the periodic table,

the scheme based on spin-pure states gradually breaks down. However, there have been no studies using molecular systems to determine how large the deviation between results of spin-pure and spin-mixed PES-based SH-AIMD calculations becomes depending on SOC strength, although there have been some reports of studies using models. In this study, we performed SH-AIMD calculations using the TFS algorithms, based on spin-pure and spin-mixed states for hydrides MH_2 (M = Si, Ge, Sn, Pb) in group 14 of the periodic table with a wide range of SOC, and systematically investigated the differences between the results given by two schemes, depending on SOC strength. Based on the initial conditions generated in the singlet ground state, we started trajectory calculations on PES of a triplet state and investigated the dynamics of the transition from the triplet state to the singlet (and vice versa) by evaluating the lifetime and rate constant of the fraction of the triplet state. First, the results of the TFS-SH-AIMD simulations show that for SiH_2 (SOC $\sim 60\ cm^{-1}$), the trajectories in the spin-pure and spin-mixed PES-based simulations exhibit similar behavior, with essentially most of the trajectories staying in the T_1 state. In the case of GeH_2 (SOC $\sim 380\ cm^{-1}$), the time evolution of the fraction of trajectories in each simulation is almost the same, as well as the lifetime, rate constant, and the electronic population. Of course, in the case of SnH_2 (SOC $\sim 900\ cm^{-1}$) and PbH_2 (SOC $\sim 3000\ cm^{-1}$), the SOC is higher than in the case of SiH_2 and GeH_2, and therefore the importance of using spin-mixed PESs is high, and the dynamics for different PES types are very different, as shown in the simulation. In particular, unlike the internal conversion, the SOC is constant over a wide coordinate space, which in the TFS-SH-AIMD simulations leads to unphysical transitions that occur in regions far from the seam of crossing in the PbH_2 case. Thus, it is clearly shown that spin-mixed PES-based simulations are essential for elementary processes involving intersystem crossings in systems containing elements after the fourth period, even if they are computationally expensive.

Chapter III

Intersystem crossing dynamics based on spin-pure and spin-mixed potential energy surfaces with Zhu-Nakamura global switching algorithm

Abstract

Surface hopping ab initio molecular dynamics (SH-AIMD) simulations based on spin-pure and spin-mixed states are performed for a series of XH_2 (X = Si, Ge, Sn, Pb) molecules, which have different spin-orbit coupling (SOC) strengths. Zhu-Nakamura (ZN) global switching algorithm was used to consider non-adiabatic transitions.

3.1 Introduction

The pioneer works on the non-adiabatic transition by Landau and Zener date back to 1932. Molecular dynamics methods were proposed in the 1950s and to date have been used to predict phenomena in physics, chemistry, and biological systems. In molecular dynamics, molecules are described by a classical equation of motion according to the gradient of a single potential surface. Non-adiabatic transitions are quantum phenomena that are common in molecular systems and can be found in various places. Surface hopping (SH) methods were proposed in the 1960s and 1970s to treat non-adiabatic transitions in classical molecular dynamics. Bjerre and Nikitin *et al.* proposed a method of bifurcating the classical orbitals into two in the non-adiabatic region in 1967. The SH method proposed by Tully and Preston in 1971 is the prototype of the widely known SH method, which determines whether a transition is possible or not by comparing a Landau-Zener non-adiabatic transition probability and a random number. However, during this initial stage, the TSH method faced a challenge when applying the Landau-Zener formula to compute non-adiabatic transition probabilities [1, 2]. This issue could potentially result in artificial transitions between states.

In 1990, Tully developed the Fewest switches algorithm, which solves the Schrödinger equation for the time-dependent wavefunction along a classical trajectory and calculates non-adiabatic transition probability based on the time-dependent wavefunction. In the same period, Zhu and Nakamura succeeded in obtaining a fully analytical quantum mechanical solution of the scattering matrix for the Landau-Zener and non-adiabatic tunneling one-dimensional two-state linear curve crossing models, which is known as the Zhu-Nakamura (ZN) theory today. The Landau-Zener formula has restrictions on the energy of the molecule or the size of the coupling strength between electronic states, while the ZN theory over-

comes these ristrictions and gives an fully analytical solution that describes non-adiabatic transitions including non-adiabatic tunneling.

The ZN theory which was originally developed for one-dimensional models has also been applied to molecular dynamics, which is a multidimensional case. The ZN theory-based SH-AIMD (ZN-SH-AIMD) method has also been developed. [125, 126] The ZN-SH-AIMD method estimates transition probabilities based only on the shape of the PES crossing regions without numerical solution of Schrödinger equation step by step along a trajectory. Therefore, the computational cost is kept low, and there is potential for application to larger molecules. Ishida, Nanbu, and Nakamura [125] developed a ZN-SH-AIMD method and applied it to the cis-trans photoisomerization of retinal, a relatively large molecular system, to discuss the dynamics of non-adiabatic transitions. Nanbu et al. [127] also developed a ZN-SH-AIMD method that explicitly takes solvent effects into account. Yu and Zhu *et al.* also developed a ZN-SH-AIMD method [126] and reported applications considering both internal conversion (IC) and intersystem crossing (ISC) processes [128–130]. In 2018, Hanasaki *et al.* [131] improved the algorithm for calculating the probability of surface hopping in the ZN-SH-AIMD method of Yu *et al.* and performed several test calculations to address the issues.

While its potential applicability is promising, the ZN algorithm is less standard than the TFS algorithm. Yue *et al.*[46] applied the TFS- and ZN-SH-AIMD methods to the *cis-trans* isomerization of azobenzene containing IC processes and obtained very similar results for both methods. For the ISC process, the ZN-SH-AIMD method has only been applied to the spin-pure state scheme, and no studies to compare the results from TFS- and ZN-based SH-AIMD simulations focusing on ISC dynamics has not yet been reported. Therefore, the purpose of this study is to determine the extent to which the ZN-SH-AIMD method can reproduce the result of TFS-SH-AIMD metho for ISC dynamics based on spin-pure and spin-

mixed potential energy surfaces through extensive comparisons between the two algorithms.

3.2 Zhu-Nakamura Global Switching algorithm

In the Zhu-Nakamura theory, the probability of classically allowed non-adiabatic transition for the one-dimensional two-state problem of Landau-Zener (LZ) and non-adiabatic tunneling (NT) type of energy crossing are given by following formulas [132, 133].

$$p^{ZN} = \exp\left(-\frac{\pi}{4\sqrt{a^2}}\sqrt{\frac{2}{b^2 + \sqrt{|b^4 \pm 1|}}}\right) \tag{3.2.1}$$

A sign (+ or -) indicates LZ or NT type of energy crossing. Effective coupling (a^2) and Effective colisin energy (b^2) parameters are given using diabatic quantities (V_{12}, $F_{1,2}$).

$$a^2 = \frac{\hbar^2}{2\mu}\frac{\sqrt{|F_2 F_1|}|F_2 - F_1|}{(2V_{12})^3} \tag{3.2.2}$$

$$b^2 = (E_t - E_X)\frac{|F_2 - F_1|}{\sqrt{|F_2 F_1|}(2V_{12})}$$

where F_1 and F_2 are the diabatic forces on two diabatic states, V_{12} is the diabatic coupling, μ is the reduced mass, E_X is the averaged potential energy at the crossing point, and E_t is the internal energy (the potential energy plus the kinetic energy). To extend the above one-dimensional forms to the AIMD simulation, Yu and co-workers proposed formulas to evaluate these two one-dimensional quantities using multi-dimensional quantities (diabatic force vectors $\mathbf{F_{1,2}}$) as follows. [126]

$$\frac{\left|F_2 - F_1\right|}{\sqrt{\mu}} = \sqrt{\sum_{i=1}^{N} \frac{1}{m_i} \sum_{\alpha=x,y,z} \left(F_2^{i\alpha} - F_1^{i\alpha}\right)^2} = \Gamma$$

$$\frac{\sqrt{\left|F_2 F_1\right|}}{\sqrt{\mu}} = \sqrt{\left| \sum_{i=1}^{N} \frac{1}{m_i} \sum_{\alpha=x,y,z} F_2^{i\alpha} F_1^{i\alpha} \right|} = \Omega \tag{3.2.3}$$

Then, a^2 and b^2 can be rewritten by using Γ and Ω as follows.

$$a^2 = \frac{\hbar^2}{2}\, \Gamma\, \Omega\, \left(2V_{12}\right)^{-3}$$

$$b^2 = \left(E_t - E_X\right)\, \frac{\Gamma}{\Omega}\, \left(2V_{12}\right)^{-1} \tag{3.2.4}$$

An important issue remains to be addressed here. The above equations are defined in terms of diabatic quantities, but in the usual use of a quantum chemistry program, diabatic quantities cannot be obtained and the diabatization procedure is not uniquely determined. Yu and co-workers proposed a method to get approximate diabatic forces ($\mathbf{F_{1,2}}$) and coupling V_{12} using adiabatic quantities (potential energies of upper/lower adiabatic states $U_{\pm}$ and their nuclear gradient), as follows.

$$F_1^{i\alpha}(t) = \frac{-1}{R_{i\alpha}(t_3) - R_{i\alpha}(t_1)} \times \left[\frac{\partial U_-}{\partial R_{i\alpha}(t_3)} \left(R_{i\alpha}(t) - R_{i\alpha}(t_1)\right) \frac{\partial U_+}{\partial R_{i\alpha}(t_1)} \left(R_{i\alpha}(t) - R_{i\alpha}(t_3)\right) \right]$$

$$F_2^{i\alpha}(t) = \frac{-1}{R_{i\alpha}(t_3) - R_{i\alpha}(t_1)} \times \left[\frac{\partial U_+}{\partial R_{i\alpha}(t_3)} \left(R_{i\alpha}(t) - R_{i\alpha}(t_1)\right) \frac{\partial U_-}{\partial R_{i\alpha}(t_1)} \left(R_{i\alpha}(t) - R_{i\alpha}(t_3)\right) \right]$$

$$V_{12}(t) = \frac{U_+(t) - U_-(t)}{2} \tag{3.2.5}$$

The diabatic force estimation algorithm by Yu *et al.* is a simple linear interpolation of adiabatic gradients along a given trajectory. Hanasaki *et al.* [131] also proposed

The method proposed by Yu and co-workers is denoted as Zhu-Nakamura global switching (GS) algorithm [134]. After hopping, velocity adjustment for total energy conservation is done according to the usual SH procedure instead of the procedure by Yu *et al*. (from eq. 13 to eq. 15 in ref [126]). In their procedure, velocity adjustment is performed in the three-dimensional space of each atom. However, regular velocity adjustment in the SH procedure is performed by scaling the component in the direction of a certain vector (usually, non-adiabatic coupling vector) in the $3N$-dimensional space of degree of nuclear freedom.

3.3 Results and Discussions

Before starting a ZN-SH-AIMD simulation, a threshold of energy difference to judge non-adiabatic transitions must be determined. **Fig. 3.1** shows tha structure distribution where the energy difference between two spin-pure or spin-mixed states is below a pre-determined energy difference threshold, color-coded in yellow. For fairness, a threshold is set to 0.3, 0.3, 0.4, and 1.0 eV for SiH_2, GeH_2, SnH_2, and PbH_2, respectively, in spin-mixed PES-based simulations so as not to limit possible transitions by a threshold, whereas it is set to 0.3 eV in spin-pure PES-based simulations.

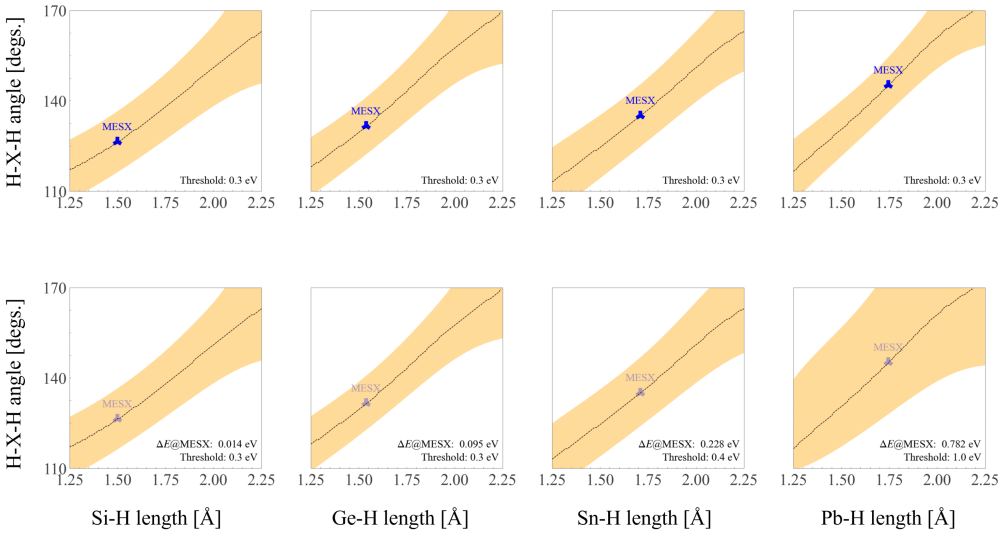

Figure 3.1. Structure distributions where the energy difference between two spin-pure or spin-mixed states is below a pre-defined energy difference threshold, colored in yellow. The value of threshold is shown at the lower right corner of the plot area in each graph.

3.3.1 Time evolution of the fraction of the triplet state of trajectories

Figure 3.2 shows the time evolution of the fraction of T_1 state (denoted by $F_3(t)$) of the trajectories where the nuclei stay in the T_1 state. [123] In order to compare the behavior of the spin-pure and spin-mixed PES-based simulations, we evaluated F_3 (t) for the spin-mixed simulation by considering the contribution of the T_1 component of the spin-mixed states along the trajectories. The fraction of T_1 state (the gray dashed line for the spin-pure PES-based simulation and the black solid line for the spin-mixed PES-based simulation) decreases over time, except for PbH_2. The time evolutions of $F_3(t)$ show qualitatively similar features between the spin-pure and the spin-mixed simulations for each molecule.

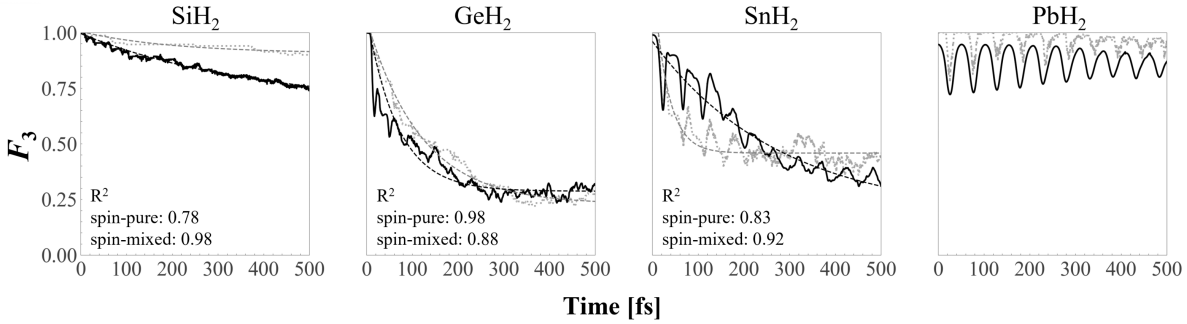

Figure 3.2. Time evolution of the fraction of trajectories staying in the T_1 state calculated from trajectory ensemble based on the spin-pure PESs (dotted gray line) and the spin-mixed PESs (solid black line), calculated from ZN-SH-AIMD simulations. In the spin-mixed PESs, $F_3(t)$ is evaluated considering the contribution of T_1 components in the spin-mixed states. A dashed line represents the fitting regression curve of each $F_3(t)$. R^2 values for each simulation (spin-pure, spin-mixed) are as follows: SiH_2: (0.78, 0.98), GeH_2: (0.98, 0.88), and SnH_2: (0.83, 0.92).

To quantitatively discuss the time evolution of the $F_3(t)$, the kinetic analysis of each $F_3(t)$ was performed as done with TFS-SH-AIMD simulations.

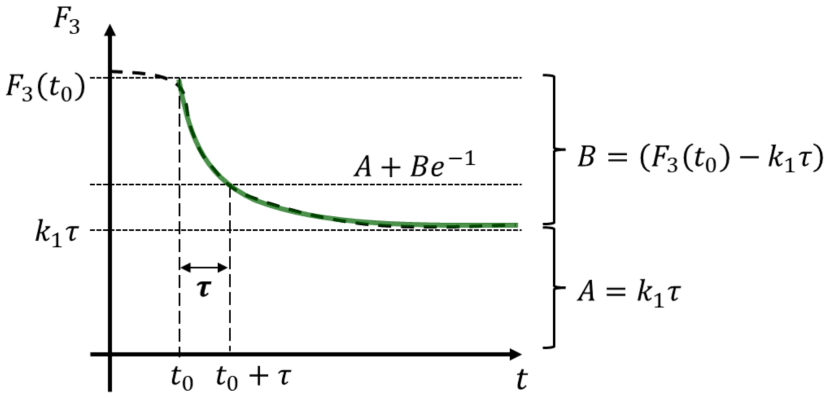

Figure 3.3. Schematic picture of $F_3\,(t)$ (dashed black line) and parameters used in kinetic analysis. For $F_3\,(t)$, a region of t t_0 (denoted by green color) was used for the fitting in kinetic analysis.

The rate constants k_1 and k_3 correspond to the ISC processes from S_0 to T_1 and T_1 to S_0, respectively, and τ represents the lifetime of the T_1 state. The value of τ was evaluated using first-order kinetics based on the following equation [123, 124].

$$F_3\,(t) = \left[F_3(t_0) - k_1\tau\right] \exp\left(-\frac{t - t_0}{\tau}\right) + k_1\tau \tag{3.3.1}$$

$$\tau = \frac{1}{k_1 + k_3}$$

For SiH_2, as shown in **Fig. 3.2**, the $F_3\,(t)$ curves show different decay features for the spin-pure and spin-mixed PES-based simulations (decreasing to 0.90 and 0.75, respectively), resulting in a large difference in lifetime (202 and 381 fs, respectively). This difference However, from the comparison with the results of TFS-SH-AIMD simulations, a spin-pure PES-based simulation is recommended in a ZN-SH-AIMD simulation for a small SOC system such as SiH_2. For SiH_2, in the spin-pure PES-based simulation, the F_3 curve of the ZN-SH-AIMD simulation is quantitatively similar to that of the TFS-SH-AIMD simulation.

In the case of GeH_2, the $F_3(t)$ curves from spin-pure and spin-mixed PES-based simulations show similar behavior, but the lifetimes and rate constants obtained by fitting show deviations as in the TFS-based simulations. For the spin-pure PES-based simulations, the lifetimes and rate constants are (119 fs, 1.93×10^{12} s^{-1}, 6.51×10^{12} s^{-1}), while for the spin-mixed PES-based simulations they are (67.5 fs, 4.24×10^{12} s^{-1}, 10.6×10^{12} s^{-1}), resulting in a difference of one order of magnitude, especially for k_3. The spin-pure PES-based ZN-SH-AIMD simulations reproduce well the previous AIMS results (119 fs, 3.1×10^{12} s^{-1}, 5.3×10^{12} s^{-1}) and the spin-pure PES-based TFS-SH-AIMD simulation (113 fs, 2.26×10^{12} s^{-1}, 6.53×10^{12} s^{-1}).

In the case of SnH_2, the $F_3(t)$ curves from the spin-pure PES-based simulations show a sharp decrease in the first 60 fs, similar to the TFS-SH-AIMD simulations, followed by a slow decrease with oscillations. Thus, the lifetime is relatively close to the results of the TFS-SH-AIMD simulations. However, in the spin-mixed PES-based simulation, the fraction decays gently with larger oscillations. The lifetimes are therefore much longer than those of the spin-pure PES-based simulation.

In the case of PbH_2, oscillations in $F_3(t)$ are observed in both simulations. Therefore, fitting the fraction curve to Eq. (7) cannot be achieved. In the spin-pure PES-based simulation, each time the molecular system passes through the S_0-T_1 crossing seam, the trajectory hops to another PES and the spin state changes, causing the fraction to oscillate. On the other hand, in the spin-mixed PES-based simulations, surface hopping does not occur, but the T_1 fraction shows oscillations due to the change in the mixing ratio of the different spin states.

Table 3.1. Parameters obtained from kinetic analysis for T_1 fraction decay

	SiH_2		GeH_2		SnH_2		PbH_2	
	spin-pure	spin-mixed	spin-pure	spin-mixed	spin-pure	spin-mixed	spin-pure	spin-mixed
τ / fs	202	381	119	67.5	31.4	280	–	–
k_1 / 10^{12} s^{-1}	4.48	1.76	1.93	4.24	14.6	0.634	–	–
k_3 / 10^{12} s^{-1}	0.463	0.862	6.51	10.6	17.3	2.94	–	–
$F_3(t_0)$	1.00	0.987	1.00	0.986	1.00	0.924	–	–

3.3.2 Distribution of the number of surface hopping against energy difference

Energy differences at hopping points and the frequencies are discussed for spin-pure and spin-mixed PES-based simulations. **Figure 3.4** shows the distribution of surface hopping versus energy difference for ZN-SH-AIMD simulations. In spin-pure PES-based simulations, the TFS algorithm allows surface hopping at points away from the seam of crossing, as shown in **Fig. 2.8a**. The TFS algorithm requires a large number of surface hopping, including unphysical hopping, to reflect drastic changes in the electronic population in systems with large SOC, for example, PbH_2, as shown in **Fig. 2.6**, violating the "fewest switches" concept [112, 113]. In contrast, the ZN-SH-AIMD method allows surface hopping only at the crossing points of singlet and triplet, as shown in **Fig. 3.4a** (global switching algorithm). Thus, the ZN-SH-AIMD algorithm avoids hopping with large energy differences that cause unphysical dynamics. Naturally, in the spin-mixed PES-based simulations, the TFS-SH-AIMD algorithm (Fig. 6b) and the ZN-SH-AIMD algorithm (Fig. 8b) show similar results,

but in the ZN-SH-AIMD simulations, the hopping occurs in a narrower region.

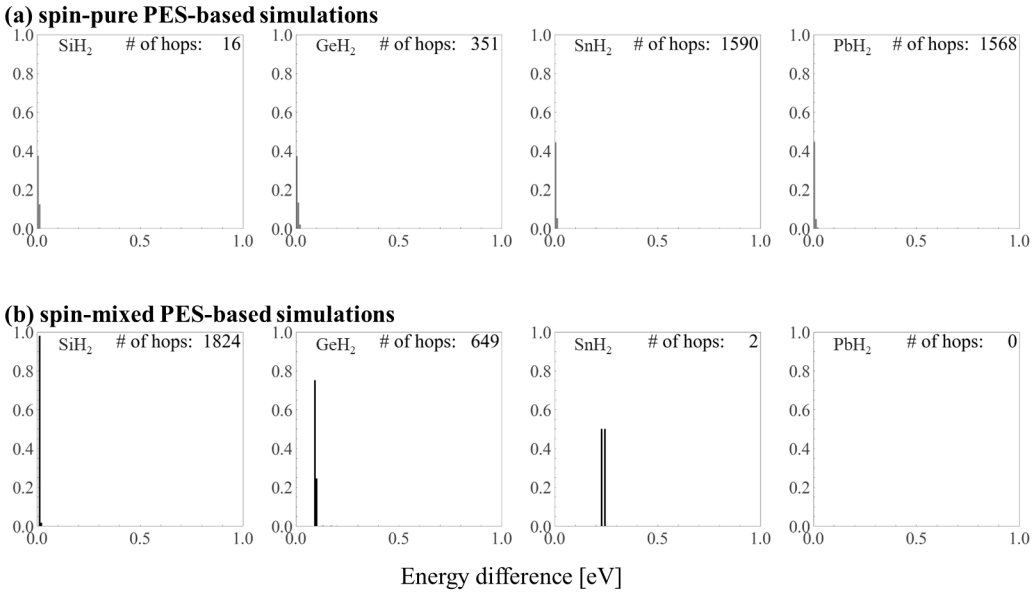

Figure 3.4. The distribution of energy differences between states when surface hopping occurs in simulations using ZN-SH-AIMD algorithm, for (a) spin-pure PES-based simulations and (b) spin-mixed PES-based simulations.

3.3.3 ISC probability

Finally, we discuss the ZN hopping probabilities in SH-AIMD simulations based on spin-pure and spin-mixed PES. The interpretation of the ZN probability is a probability a hopping occurs once a classical trajectory passes through a crossing point. **Fig. 3.5** shows ISC probabilities at hopping points in spin-pure (gray) and spin-mixed (black) PES-based ZN-SH-AIMD simulations. Except for PbH_2, the probability of ISC is higher in spin-mixed PES-based simulations than in spin-pure PES-based simulations. This subtle difference can be attributed to the GS algorithm used in this simulation. The GS algorithm uses the diabatic expression to determine the parameters a^2 and b^2, which are necessary for calculating tran-

sition probabilities in the ZN theory. Zhu and Nakamura also proposed formulas to compute the above two parameters based on adiabatic potential energy surfaces. However, multi-dimensional formulations have not proposed so far. If the ZN adiabatic multi-dimensional formula is available, more discussion of this issue would be possible.

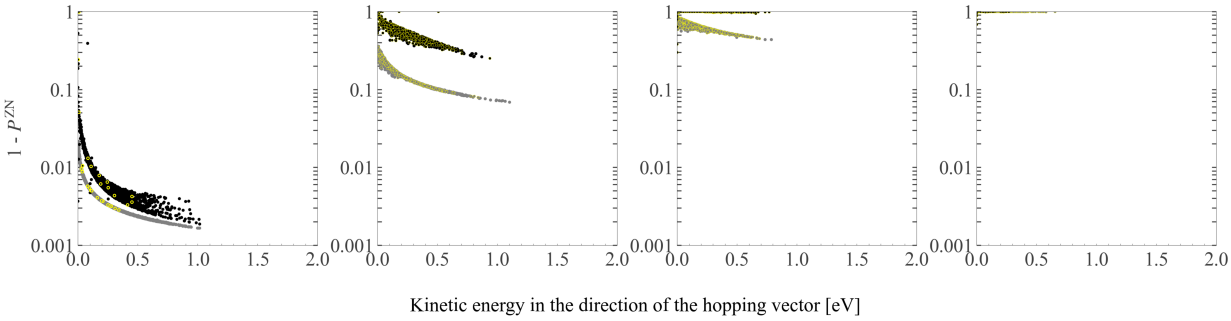

Figure 3.5. ISC probability against the kinetic energy at a hopping point in spin-pure (gray) and spin-mixed (black) PES-based ZN-SH-AIMD simulations. The highlighted dots indicate that an ISC occurred.

3.4 Conclusion

In non-adiabatic molecular dynamics study, which began with the pioneering works of Landau and Zener, Tully's fewest switches (TFS) algorithm based on the time evolution of the electronic wavefunction has been widely used in the framework of SH-AIMD method, but in recent years, the Zhu-Nakamura (ZN) theory-based (ZN) algorithm, which computes a transition probability based on the shape of potential energy surfaces, has been increasingly used. The TFS algorithm is computationally expensive because it requires non-adiabatic couplings and spin–orbit couplings along the time evolution of the nucleus each time to propagate the electronic wavefunction, and it is often limited in its use by the limited number of electronic structure calculation methods that can calculate the non-adiabatic coupling vector. On the

other hand, the ZN algorithm estimates a transition probability using basically information on the shape of potential energy crossing, thus the limitations and computational costs of electronic structure calculations are clearly smaller that those of the TFS algorithm. Hence, the ZN algorithm is expected to be applied for systems to which the TFS algorithm could not be applied.

However, contrary to its potential applicability, the ZN algorithm is not standard compared to the TFS algorithm. As far as internal conversion dynamics, it has been shown that two algorithms give quite similar results, but no such report or investigation on intersystem crossing dynamics. Extensive comparisons in this study show that TFS-SH-AIMD and the ZN-SH-AIMD simulations basically show qualitative agreement for ISC dynamics with a wide range of SOC, although the ZN-SH-AIMD method does not require a nonadiabatic coupling term, significantly reducing the computational cost compared to the TFS-SH-AIMD method. Furthermore, its versatility/simplicity that ZN algorithm basically requires only the information of potential energy surfaces is a huge advantage, even considering the tradeoff with quantitative accuracy. The present results suggest that the less expensive ZN-SH-AIMD can be successfully utilized to investigate the dynamics of photochemical reactions based on quantum chemical calculations.

It is found that ZN algorithm has a certain accuracy with efficiency, but further quantitative improvements can be expected. The original ZN theory in one-dimensional model provides two expressions to evaluate a transition probability: diabatic and adiabatic expressions based on diabatic and adiabatic representations of potential energy surfaces respectively. However, only the diabatic expression have been extended to multi-dimensional case for the use in SH-AIMD simulations and approximate diabatic properties to determine a transition probability is required in SH-AIMD simulations with adiabatic representation. Those diabatization could cause some numerical errors and it is more natural to obtain a transition

probability from adiabatic expression in SH-AIMD simulation with adiabatic representation. Therefore, the development of a scheme to obtain transition probabilities using the adiabatic expression should be addressed in the future work.

Chapter IV

Excited-State Intramolecular Proton Transfer and subsequent dynamics of *ortho*-nitrophenol

Abstract

Excited-state dynamics involving non-adiabatic transition of ortho-nitrophenol was investigated.

4.1 Introduction

A 2-substituted benzene derivative has three distinct positional isomers (*para*, *meta*, and *ortho*), according to the relative position of the two substituents. For nitrophenol, in the *ortho*-nitrophenol (*o*-NP), where the hydroxy and the nitro groups are next to each other, an intramolecular hydrogen bonding can be formed between the two substituents, which

distinguishes *o*-NP from other nitrophenols (e.g., melting point, vapor pressure, reactivity, and charge distribution).

The intramolecular hydrogen bonding contributes to not only the stability of the ground state but also changes the properties of the molecule in the excited states. The A-band absorption of *o*-NP is a unique new band, located around a lower range than those of phenol, nitrobenzene [135] and other nitrophenols [136]. This A-band excitation is originated from an intramolecular charge transfer ($\pi\pi^*$) excitation mainly involving the π orbital at the benzene ring and π^* orbital at the nitro group, determined by using quantum chemical calculations [135]. That is similar to those of the nitrobenzene, but each orbital of *o*-NP is more delocalized over the entire molecule. Thus, intramolecular hydrogen bonding is not just an interaction between functional groups but an interaction over the entire molecule, including the benzene ring. It is also noteworthy that *o*-NPs with intramolecular hydrogen bonds are isomerized by proton transfer in the excited state. This process is called excited-state intramolecular proton transfer (ESIPT) and it is considered an important process in organic electroluminescence (EL), photostability of drug molecules, and biochemical systems [137]. *o*-NP is one of the smallest and the most basic molecules that undergo ESIPT.

o-NP is also of interest in atmospheric chemistry. Nitrophenols are pollutants widely abundant in a variety of environments (forest, rural, urban, and marine areas), both in gaseous and condensed phases [138, 139]. Due to its strong absorption in a UV-A region, the photodissociation of *o*-NP is considered as a source of nitrous acid (HONO) [140, 141]. HONO is a precursor of OH radical [142, 143], a chemical species that is important as a basis for chemical reactions in the atmosphere. Therefore, the photoreaction mechanism of the *o*-NP molecule is essential for understanding atmospheric chemistry processes.

The photoexcitation reaction of *o*-NP has been investigated experimentally and theoretically. In particular, experimental studies using time-resolved techniques to capture ul-

trafast excited dynamics are noteworthy. The work by Takezaki *et al.* [144] is the earliest time-resolved study of excited-state dynamics of *o*-NPs and was the first to point out that after excitation by UV light, the molecule relaxes to the first excited triplet state via intersystem crossing (ISC). Based on their implication, the reaction pathway in the triplet potential energy surface was theoretically investigated, and it was shown that HONO dissociation is more likely to occur in T_1 than at S_0 state [145, 146]. Ernst *et al.* investigated the relaxation dynamics of *o*-NP by time-resolved photoemission spectroscopy (TRPES) in the gas phase and transient absorption spectroscopy (TAS) in the liquid phase using ultraviolet (UV) and visible laser pulses, and proposed fast relaxation via internal conversion (IC) from S_1 to S_0 state and a HONO split-off in the triplet manifolds via ISC from S_1 to T_1 state [147]. Xu *et al.* [128, 148] theoretically investigated isomerization reaction, including ESIPT in the ground and excited states, and showed relaxation processes through triplet states to the ground state with/without ESIPT, while the mechanism of HONO dissociation was not addressed. Nitta *et al.* investigated the A-band excitation dynamics using TRPES and confirmed ultrafast HONO formation at 400 $\sim$ fs. In several time-resolved experiments with quantum chemical calculations, several dissociation channels for different products have been postulated in the triplet states [147, 149–153], however, the definitive mechanism remains unclear.

Time-dependent density functional theory is widely used to study molecular or solid systems. In conventional TDDFT, excited states were described as a response state referencing the ground state. Thus, it breaks down near a conical intersection between the ground and the first excited states. Spin-flip (SF-) TDDFT overcomes the limitation by using a high spin state as a reference state, for example, the T_1 state for singlet ground and excited states. However, the spin-flip method suffers from spin-contamination due to its spin incompleteness [77], and it sometimes makes it difficult to perform geometry optimization,

reaction path calculation, or molecular dynamics simulation [78, 79]. Recently, Lee, Choi, and co-workers have developed the mixed-reference SF-TDDFT (MRSF-TDDFT) [80, 81]. MRSF-TDDFT avoids spin-contamination by using a mixed-reference reduced density matrix and has been successfully applied to non-adiabatic molecular dynamics with Tully's fewest switches (TFS) algorithm [22] in the gas and liquid phase [83–85].

In this study, we perform non-adiabatic molecular dynamics simulation with the MRSF-TDDFT and the ZN global switching algorithm for the excited state reaction of *o*-NP. The excited state reaction of *o*-NP is complex, involving ESIPT, internal conversion (IC), intersystem crossing (ISC), and dissociation processes in a very short period of time (sub-picosecond). Previous studies have focused on reaction mechanisms on the triplet surface, while the fast relaxation via IC between the S_0 and the S_1 state after ESIPT is also predicted, and the reason for the competition between IC and ISC is unclear. Therefore, the motivation for this study is the theoretical understanding of the ultrafast excited state dynamics of *o*-NP, which has been assumed to involve ESIPT, IC, and ISC prior to the dissociation process.

4.2 Computational Details

4.3 Results and Discussion

In this study, several electronic structure theories implemented in different electronic structure software were used. GAUSSIAN 16 software revision C.01 [154] was used for Time-Dependent (TD) DFT calculations with several functionals. GAMESS(US) software version 2022 R2 [155] was used for mixed-reference spin-flip (MRSF) TDDFT [80, 81] calculations with Becke's half-and-half exchange and Lee–Yang–Parr correlation (BHHLYP) functional.

OpenMolcas version 23.06 [156] were used for extended multi-state complete active space second-order perturbation theory (XMS-CASPT2) [58, 63] calculations. The computational details will be noted each time the results are presented.

Figure 4.1 shows the molecular structure of *o*-NP.

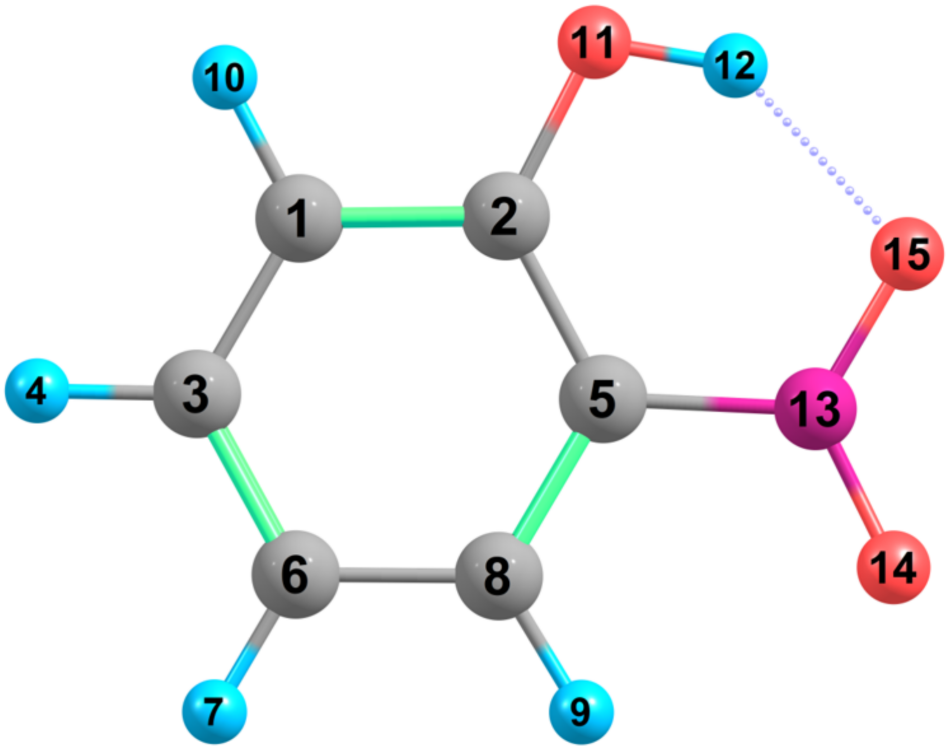

Figure 4.1. *ortho*-nitrophenol

4.3.1 Franck-Condon excited states

Table 4.1 shows the excitation energy and oscillator strength of the S_1 state at the equilibrium structure of the ground state.

Table 4.1. Vertical Excitation energy (E^{exc}) in eV and oscillator strength (f) of the first excited state of *ortho*-nitrophenol.

Method	APFD[a]	CAM-B3LYP[a]	ωB97XD[a]	LC-BLYP[a]	CASSCF[b]
E^{exc} / eV	3.51	3.89	3.91	4.12	4.35
f	0.0580	0.0926	0.0935	0.0000	0.0000
Method	SCS-CC2[c]	CC2[c]	ωB97X[c]	M06-2X[c]	B3LYP[c]
E^{exc} / eV	4.08	3.97	4.07	4.00	3.38
f	0.0580	0.0926	0.0935	0.0000	0.0763

[a] 6-31G+(d)

[b] See ref. [148]

[c] See ref. [157]

Ab initio coupled-cluster method and DFT shown in **Fig. 4.1** and ref. [157] basically predict that the S_1 state of *o*-NP has a $\pi\pi^*$ excitation character while a few cases of DFT calculation predict $n\pi^*$ excitation character. The mixed-reference spin-flip (MRSF) TDDFT using GAMESS(US) and the multi-configurational perturbation theory (XMS-CASPT2) were also employed to compute excitation energies and oscillator strengths of low-lying singlet excited states. Geometry optimization in the S_0 state was performed at each level of theory. Exci-

tation energies and oscillator strengths are shown in Table 4.2. The optimized structure at the MRSF-TDDFT level is in C_S symmetry while the one at XMS-CASPT2 is in near C_S symmetry.

Table 4.2. Vertical Excitation energies and oscillator strengths of low-lying singlet excited states of *ortho*-nitrophenol. cc-pVDZ basis set was used in both computations.

Method/STATE	S_1	S_2	S_3	S_4
MRSF-TDDFT	4.43 (0.28)	5.18 (0.32)	5.51 (0.00)	5.78 (0.00)
XMS-CASPT2	4.05 (0.13)	4.28 (0.05)	4.82 (0.20)	5.96 (0.07)

4.3.2 Excited-State Intramolecular Proton Transfer pathway

The reaction pathway from the Franck-Condon point in the S_1 state was calculated using MRSF-TDDFT/cc-pVDZ level of theory. **Figure 4.2** shows profiles of electronic energies and internal coordinates along the reaction pathway. r indicates a distance between two atoms and a indicates torsion or rotation angle related to the HONO group. Angle a is defined as a function of dihedral angle d as follows:

$$a = f(d) = sign(d) \times 180 - d \tag{4.3.1}$$

Three angles were chosen to characterize the excited-state reaction pathway and dynamics of *o*-NP.

$$\begin{aligned} \text{Twist of the HONO around the C-N bond: } a^{\text{twist, HONO}} &= f(d_{\text{C2C5N13O14}}) \\ \text{Pyramidalization of the HONO: } a^{\text{pyr, HONO}} &= f(d_{\text{C5N13O14O15}}) \\ \text{Swing motion of the transferring proton: } a^{\text{swing, H}} &= f(d_{\text{O14N13O15H12}}) \end{aligned} \tag{4.3.2}$$

The first step (Reaction coordinate 1.5 Å$amu^{1/2}$) in the reaction pathway is associated with the ESIPT of in-plane motion, whereas the second is associated with the HONO twist of out-plane motion. Along the ESIPT process, the S_1 energy decreases without a reaction barrier. The previous study using the CASSCF//MRCI level of theory predicted an energy barrier for proton transfer because the S_1 state in their calculation is $n\pi$ state [148]. In our calculation, the S_1 state preserves its character as $\pi\pi*$ state through the ESIPT pathway. The energy of S_2 ($n\pi$*) increases along the ESIPT pathway. From the reaction pathway calculation, S_1 state dynamics is expected to proceed fast along with the ESIPT coordinate while slow along with the HONO twist coordinate. The reaction pathway from the Franck-Condon

point at the MRSF-TDDFT level of theory is quite similar to that at CASPT2 [150]. Thus, MRSF-TDDFT is expected to qualitatively reproduce the result of CASPT2 in dynamics simulations.

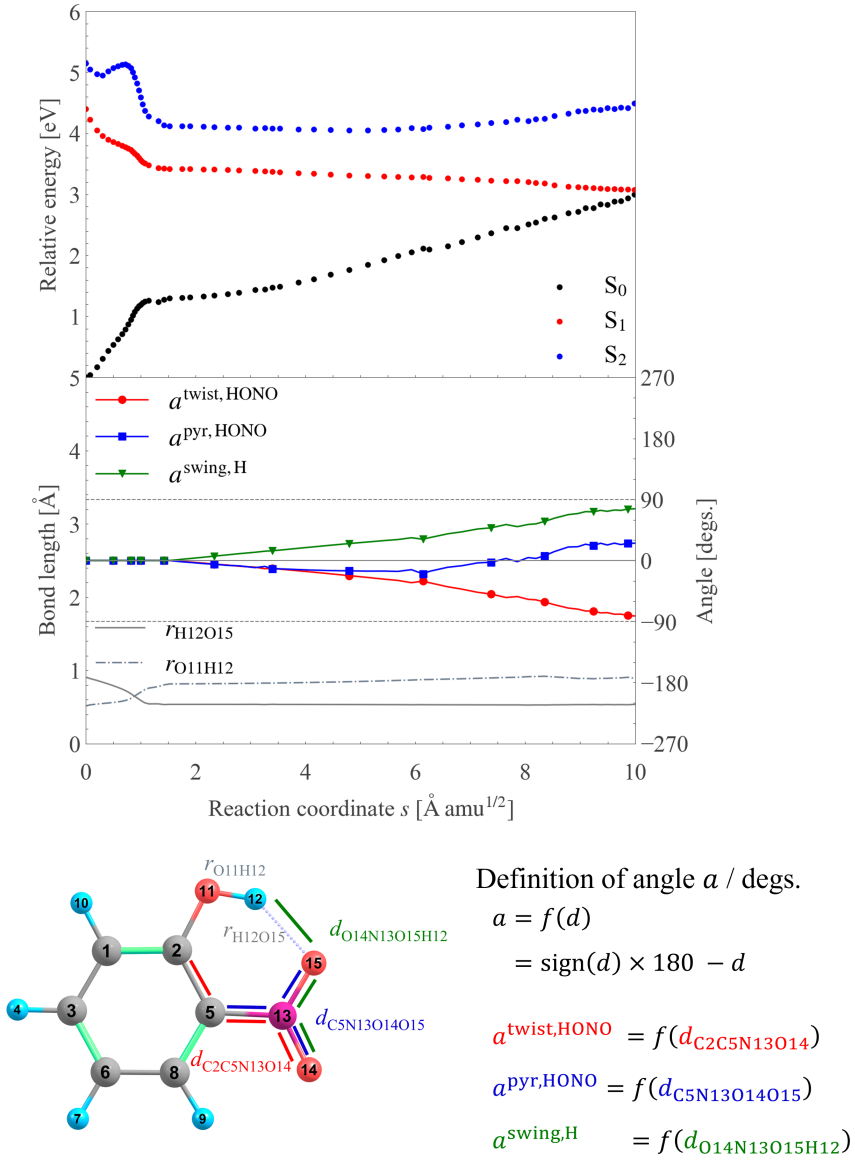

Figure 4.2. profiles of electronic energies and internal coordinates along the reaction pathway from the Franck-Condon point in the S_1 state at the MRSF-TDDFT/cc-pVDZ level of theory.

4.3.3 Minimum energy structure on the conical intersections

Optimized geometries on the conical intersection between S_0 and S_1 potential energy surfaces are shown in **Figure 4.3**. Potential energies were calculated by the MRSF-TDDFT/cc-pVDZ level of theory. MECIs were optimized using GRRM17 interface to the GAMESS(US) version 2022R2. For the MECI-1, the twist around the C-N bond ($a^{\text{twist, HONO}}$) is -85.7°and the distance between the proton and the O atom of the carbonyl group (a_{O11H12} = 1.75 Å) is kept within the hydrogen bonding distance (2 Å). A similar geometry to the MECI-1 was reported in the previous study [147]. The last geometry on the reaction pathway in the S_1 state (r_{O11H12} = 1.69 Å, r_{H12O15} = 0.991 Å, $a^{\text{twist, HONO}}$ = -82.8°, $a^{\text{pyr, HONO}}$ = 26.7°, $a^{\text{swing, H}}$ = 76.3°) reaches nearby the MECI-1. Therefore, the MECI-1 could be a main decay pathway from the S_1 state to the S_0 state. A geometry similar to the MECI-1 **Fig. 4.3a** was obtained in the previous study [147]. On the other hand, for the MECI-2, the HONO group forms almost *cis*-form ($a^{\text{swing, H}}$ = 176.6°), thus, the hydrogen bonding no longer exists.

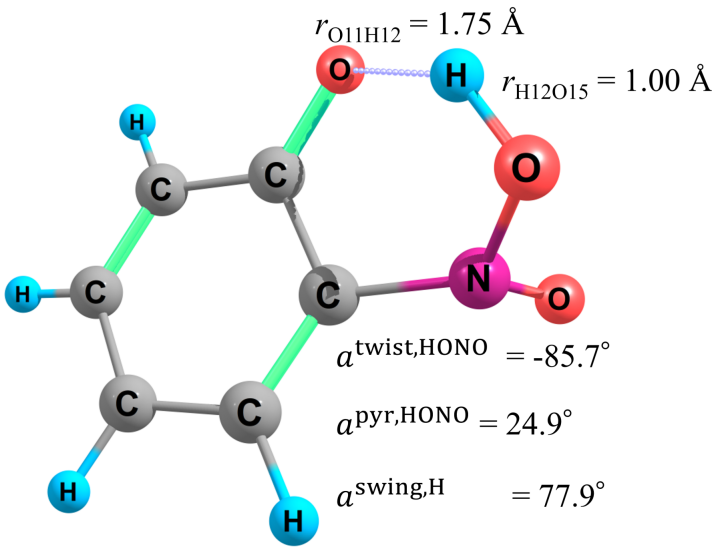

(a) MECI-1

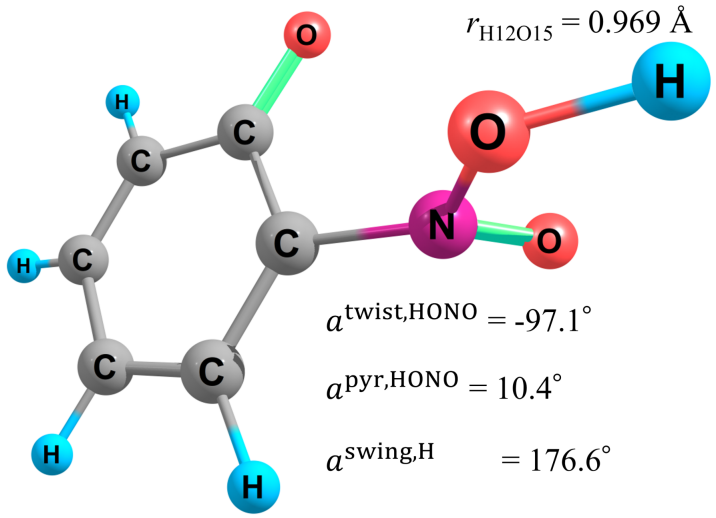

(b) MECI-2

Figure 4.3. Local minima on the conical intersection between S_0 and S_1 states

4.3.4 Non-adiabatic Molecular dynamics

Non-adiabatic molecular dynamics simulation was performed using the MRSF-TDDFT level of theory. One hundred initial conditions were generated based on Boltzmann distribution at 300 K. Nuclear coordinates and velocities were evolved up to 500 fs using the velocity-Verlet method with a time step of 0.5 fs. Non-adiabatic transitions were taken into account by using Zhu-Nakamura global switching algorithm [126]. It is not easy to choose an appropriate level of theory that can consider ESIPT, IC, ISC and dissociation with singlet and triplet states at once. Thus, in this simulation, we first focus on ESIP and IC dynamics, which are considered to occur in the early stage of this photoreaction [147, 150], and then consider the involvement of triplet states afterward. In all trajectories, ESIPT occurred within the first 20 fs. After ESIPT, trajectories branched three types of pathways. **A**. Hop to the S_0 state and back to *o*-NP, **B**. Hop to the S_0 state and keep the HONO group, and **C**. Stay on the S_1 state up to 500 fs. Some trajectories on the path **A** suddenly stopped due to the SCF convergence error which cannot be solved so far. The branching ratio is 13:28:59. **Fig. 4.4, 4.5, 4.6** shows an example of the three types of classical trajectory, with energy profiles on the upper column (S_0: black, S_1: red, S_2: blue, highlighted line: the potential surface where nuclei stay) and the internal coordinate variation (interatomic distance r and angles a) on the lower column are shown. (See Eq. 4.3.1 and 4.3.2 for the meaning of each internal coordinate). In path A, after ESIPT (as r_{H12O15} get close to 1 Å), the energy of the ground state increases by 2 eV, and as the subsequent HONO twist proceeds (as $a^{\mathrm{twist,\,HONO}}$ get close to 90 °), the energies of the S_1 and S_0 states become close to each other. Then, a non-adiabatic transition from S_1 to S_0 state occurs at $a^{\mathrm{twist,\,HONO}} \approx 90$ °, followed by back proton transfer. The average decay time is 308 fs. In path B, processes are the same as in path A until a non-adiabatic transition occurs. After the transition, the HONO keeps its bonding and continues the twist motion.

The average decay time is 328 fs, slightly shorter than that of path A. (See **Fig. 4.7**) In path C, a trajectory continues to stay in the S_1 state and the motion of the transferring proton is more pronounced than in other cases due to the switching S_1 state from $\pi\pi^*$ to $n\pi^*$ excitation character. The twist of the HONO group is relatively smaller than in other cases, thus *o*-NP cannot reach to MECIs at $a^{\text{twist, HONO}} \approx 90°$.

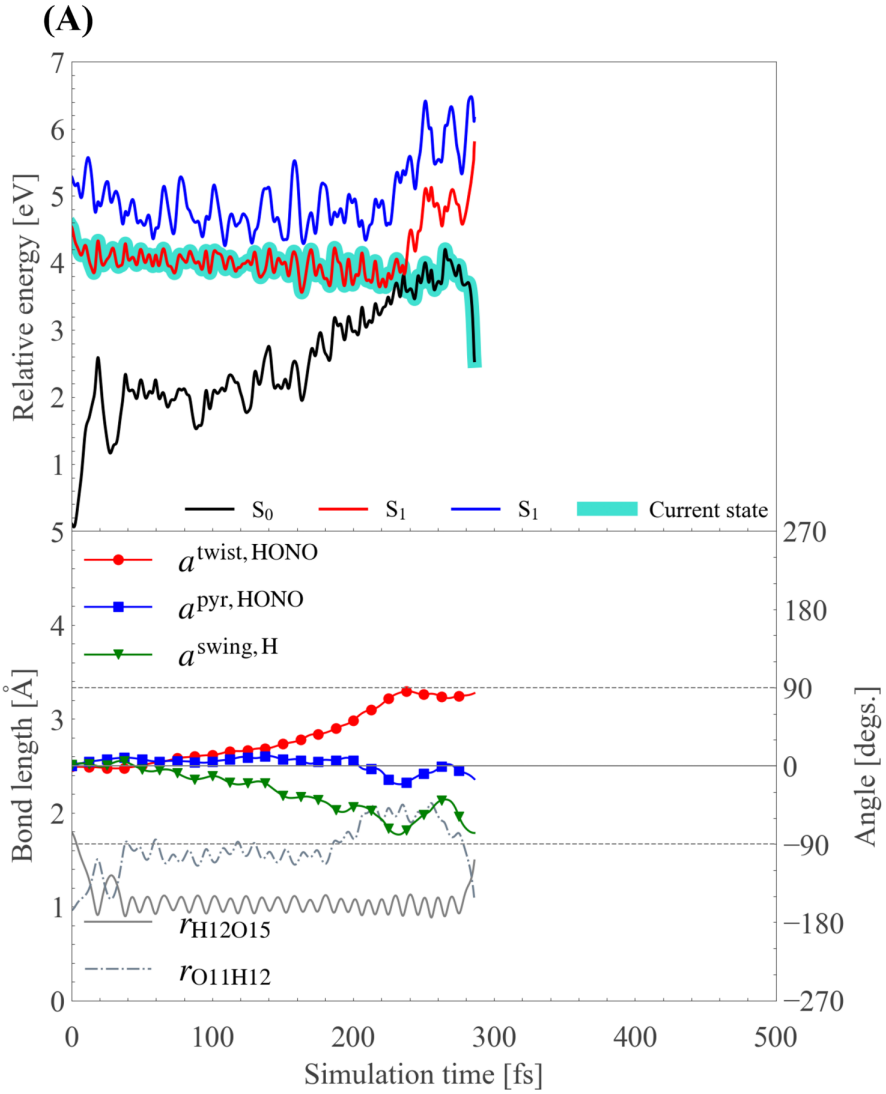

Figure 4.4. Time evolution of potential energies and internal coordinates along a trajectory of type A. Black, red, and blue solid lines in the upper column represent the potential energies of S_0, S_1, and S_2 states, respectively. The line covered with sky blue represents the state where nuclei stay. Internal coordinates are shown in the lower column: Two interatomic distances between the transferring H atom at the hydroxy group and two O atoms at the hydroxy and the nitro groups, respectively (gray dash-dot for r_{O11H12} and gray solid for r_{H12O15}), and three angles representing the HONO twist (red, $a^{\mathrm{twist,\,HONO}}$) the HONO pyramidalization (blue, $a^{\mathrm{pyr,\,HONO}}$) and the swing motion of transferring H atom (green, $a^{\mathrm{swing,\,H}}$)

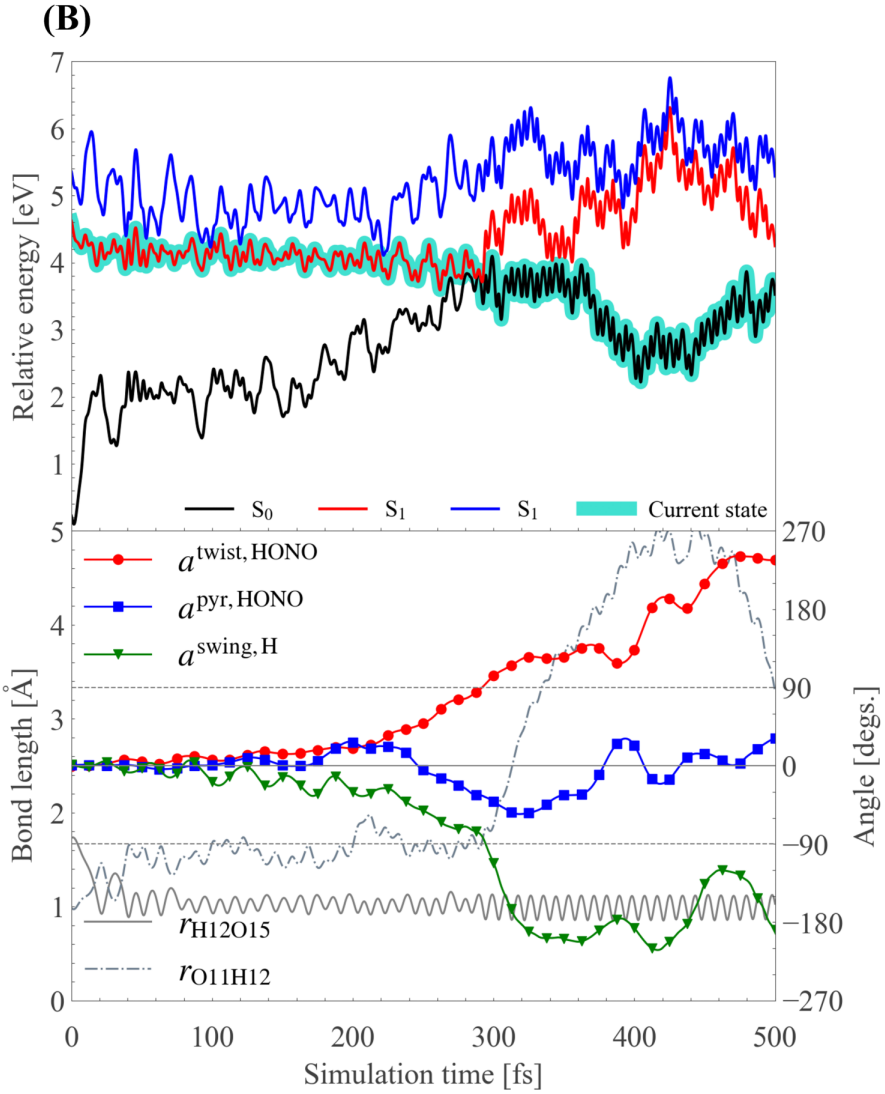

Figure 4.5. Time evolution of potential energies and internal coordinates along a trajectory of type B. Black, red, and blue solid lines in the upper column represent the potential energies of S_0, S_1, and S_2 states, respectively. The line covered with sky blue represents the state where nuclei stay. Internal coordinates are shown in the lower column: Two interatomic distances between the transferring H atom at the hydroxy group and two O atoms at the hydroxy and the nitro groups, respectively (gray dash-dot for r_{O11H12} and gray solid for r_{H12O15}), and three angles representing the HONO twist (red, $a^{\text{twist, HONO}}$) the HONO pyramidalization (blue, $a^{\text{pyr, HONO}}$) and the swing motion of transferring H atom (green, $a^{\text{swing, H}}$)

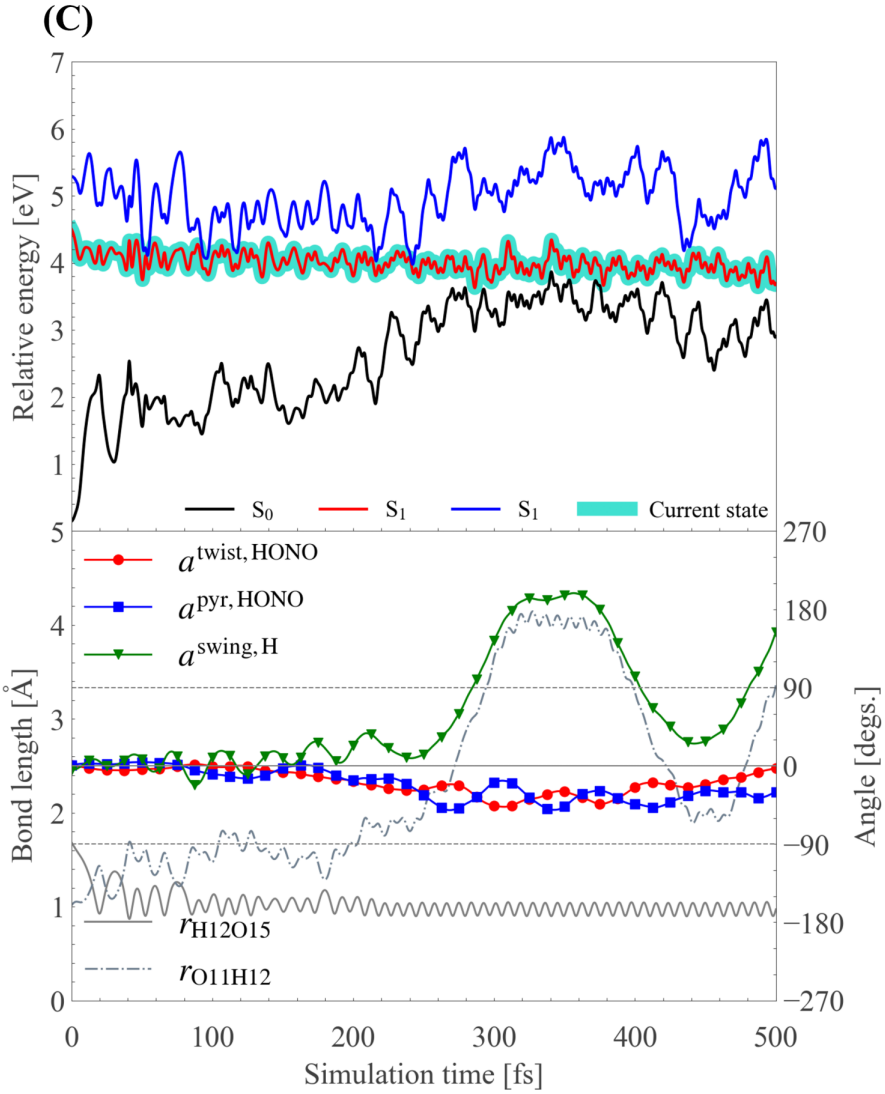

Figure 4.6. Time evolution of potential energies and internal coordinates along a trajectory of type C. Black, red, and blue solid lines in the upper column represent the potential energies of S_0, S_1, and S_2 states, respectively. The line covered with sky blue represents the state where nuclei stay. Internal coordinates are shown in the lower column: Two interatomic distances between the transferring H atom at the hydroxy group and two O atoms at the hydroxy and the nitro groups, respectively (gray dash-dot for r_{O11H12} and gray solid for r_{H12O15}), and three angles representing the HONO twist (red, $a^{\text{twist, HONO}}$) the HONO pyramidalization (blue, $a^{\text{pyr, HONO}}$) and the swing motion of transferring H atom (green, $a^{\text{swing, H}}$)

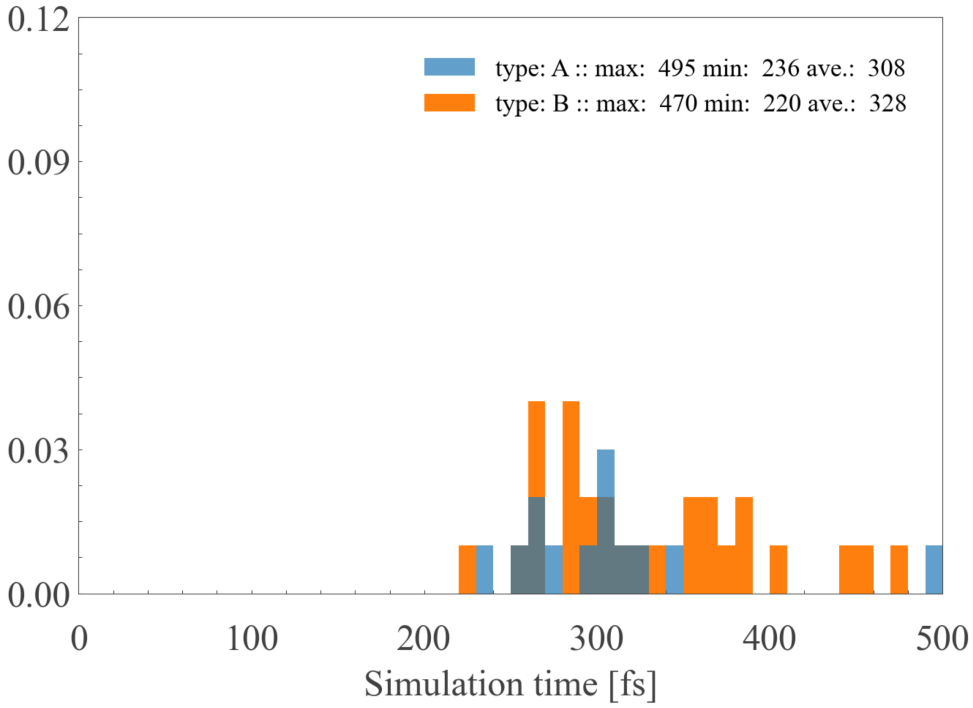

Figure 4.7. Distribution of decay time from S_1 to S_0 state.

One important point in the above dynamics simulation is that the decay to the ground state takes about 300 fs. In the time-resolved photoemission spectra of Ernst *et al.* [147], there is a spectral rise centered at 100 fs in the 1 eV range of photoelectron kinetic energy. They also found a time constant of 130 $\pm$ 10 fs for this early rising peak, which is interpreted as an internal conversion from the excited state to the ground state. Nitta *et al.* found a peak in the photoelectron spectrum (5.55 7.41 eV) that rises within 100 fs and has a time constant of 60 ± 10 fs, which roughly supports the fast internal conversion predicted by Ernst *et al.* Nitta *et al.* also found a peak centered at 250 fs in the 10.85 11.30 eV range of photoelectron kinetic energy. However, according to our calculations, the ESIPT occurs fast (around 20

fs), whereas the relaxation to S_0 takes around 300 fs. This is consistent with the fact that the gradient of the HONO twist is very small while the gradient of the ESIPT process is steep in the reaction path from the Franck-Condon point. In addition, the energy transfer between the ESIPT (in-plane motion) and the HONO twist (out-plane motion), which are orthogonal to each other, is difficult in terms of dynamics, resulting in the slow decay to the S0 state. Therefore, a new interpretation is needed to fill the discrepancy between the experimental interpretation and the computational results in this study.

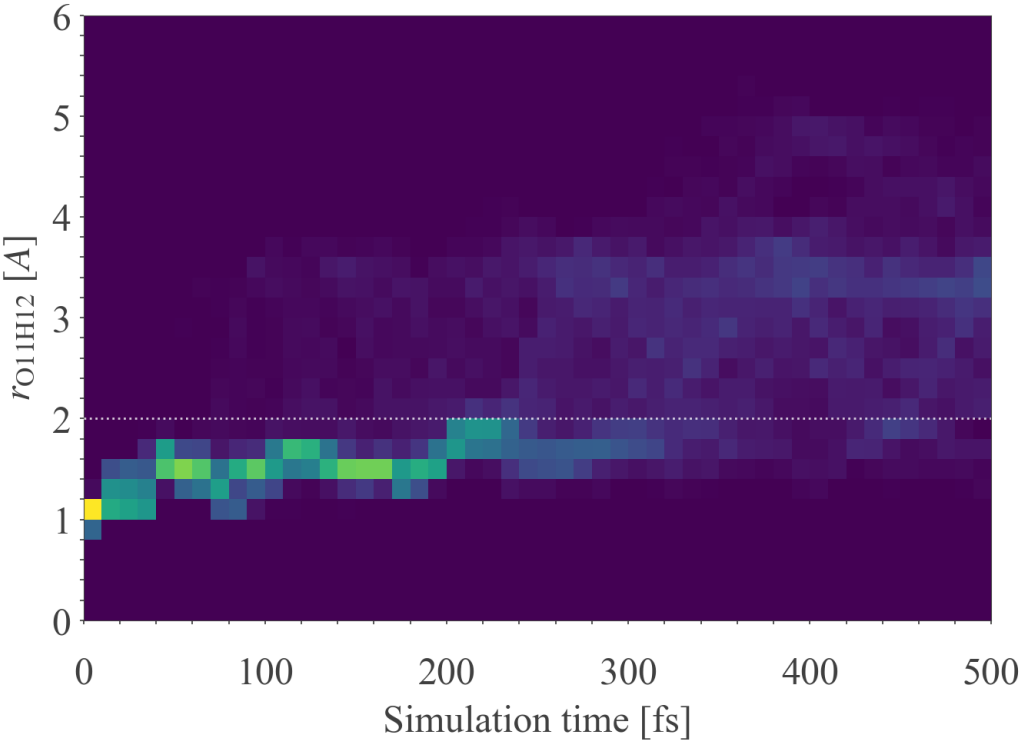

Figure 4.8. Heatmap of the interatomic distance r_{O11H12}

One of the main characteristics of this molecule is its strong hydrogen bonding. **Figure 4.8** shows a heat map of the distance between the carbonyl oxygen and the transferring

proton. 1) The first proton transfer occurs within 20 fs and the proton moves between the oxygens until about 40 fs. 2) After that, the bond between the transferring proton and oxygen at the nitro group is stabilized, keeping hydrogen bonding between the transferring proton and carbonyl oxygen until approximately 240 fs. During this time, the number of classical trajectories in which r_{O11H12} exceeds the hydrogen bonding distance of 2.0 Å (dotted line) gradually increases. 3) After 240 fs, the strength of the heatmap within 2.0 Åweakens. The first step is a proton transfer process which is a common process in every dynamics pathway. The second one is considered a deterministic process after proton transfer. In this process, an energy transfer to the HONO twist/pyramidalization or proton swing motion. After 240 fs ∼, trajectories branched into three dynamical pathways (A, B, and C).

Figure 4.9 shows the distribution of the time when r_{O11H12} first exceeds the hydrogen bond distance of 2.0 Åfor each type of trajectory. For type A which returns to *o*-NP, in a few trajectories (4 out of 12) r_{O11H12} hydrogen bond breaks then, recover the bond. A trajectory of type B keeps the hydrogen bond for a long time, while a trajectory of type C loses the hydrogen bond early after the ESIPT. The distribution of types B and C is clearly different. The distribution of Type B in **Fig. 4.9** is similar to that of the decay time to the S_0 state. The shortest hydrogen bond breaking time for Type C is 43 fs and the average is 181 fs. This shows that the bifurcation to pathway C occurs at an earlier stage than the other pathways. As we have shown, r_{O11H12} is well suited to characterize the dynamic pathways and is closely related to the hydrogen bonding that indirectly characterizes the ground state of o-NP. Therefore, it is quite possible that a mechanism such as that discussed based on **Fig. 4.8 and 4.9** appear in the experimental spectra.

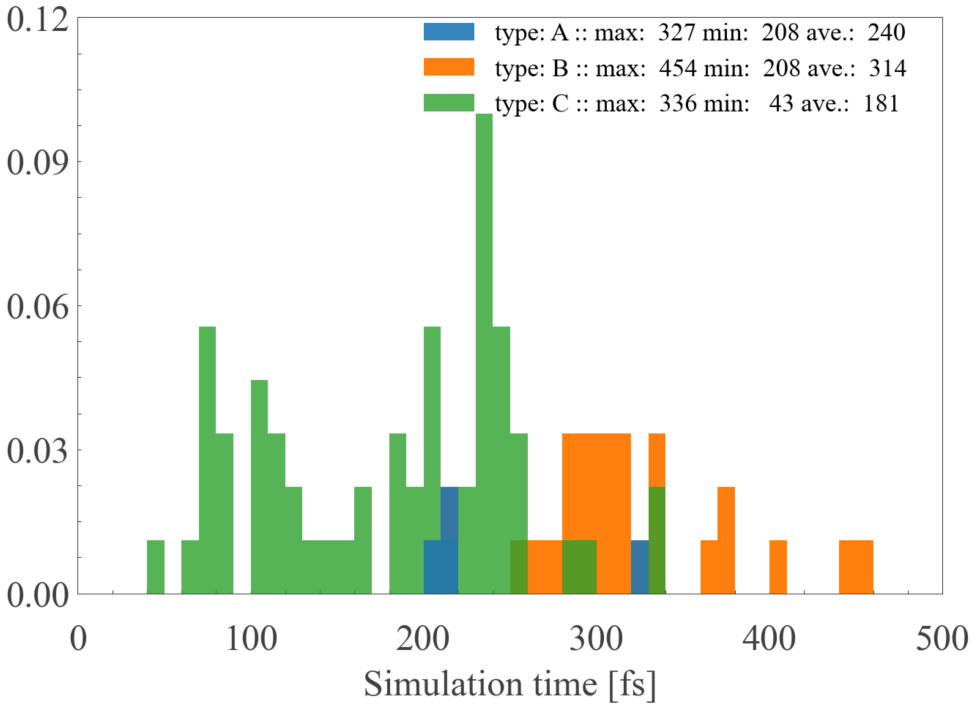

Figure 4.9. Distribution of hydrogen bond breaking time (when r_{O11H12} becomes larger than 2 Å) for each type of trajectory. Color blue, orange, and green represent trajectory types A, B, and C, respectively. In Eight, one, and three trajectories of each type, the r_{O11H12} distance is kept within 2 Å in the whole simulation time, thus data of them are not included in this figure.

In the above non-adiabatic molecular dynamics simulation, only the singlet states have been considered. The dissociation process of *o*-NP has been considered to involve the triplet state [128, 144, 147, 148, 150]. Here, to investigate the possibility of intersystem crossing in each type of trajectory. potential energies of triplet states were calculated along the trajectory and shown in **Figure 4.10**. For ease of viewing, the singlet state is shown with increased transparency, and the triplet state is shown in magenta. The lines covered with sky blue represent the electronic states in which the nuclei stay as in **Fig.4.10**. In a trajectory

of type A (top panel), the triplet state intersects only once after ESIPT before a transition to the ground state. Nitta *et al.* [150] reported that the SOC of o-NP is very small, thus, the possibility of intersystem crossing is infinitesimally small for a small number of crossings as in Type A. In addition, a classical trajectory of type A decays to the ground state and then back to the o-NP, so the possibility of a subsequent crossing to the triplet state is also small. Therefore, the possibility of intersystem crossing in type A can be ignored.

In a trajectory of type B, the triplet state approaches the current electronic state (covered by sky blue) even before the transition to the ground state, and the singlet and triplet states cross each other for some time. At this time, the hydrogen bond is gone. After a while, the triplet state leaves the singlet state, but its structural factors are not clear. Nevertheless, a classical trajectory of type B is more likely than that of type A to undergo interterm crossing.

In a trajectory of type C, triplet states approach the current electronic state of $n\pi^*$ excitation character after the hydrogen bond disappears. The T_2 state, which is energetically closest to the S_1 state, also has a $n\pi^*$ excitation character while the T_1 state has a $\pi\pi^*$ excitation character. From the viewpoint of the El-Sayed rule, intersystem crossing between singlet and triplet states with a similar character is less likely to occur. Two triplet states can exchange their characters along dynamics, thus, in a trajectory of type C, intersystem crossing may be the most likely to occur in the three types. To fully understand the photochemical reaction of *o*-NP involving the dissociation process, it is necessary to perform non-adiabatic molecular dynamics including both singlet and triplet states. The spin-orbit coupling (SOC) is key for the ISC process, and a new MRSF-TDDFT code has been developed to calculate the SOC and may be opened soon. The Zhu-Nakamura global switching algorithm has been applied to the ISC dynamics [128, 130]. Therefore, non-adiabatic dynamics simulation with singlet and triplet states will be addressed in the near future.

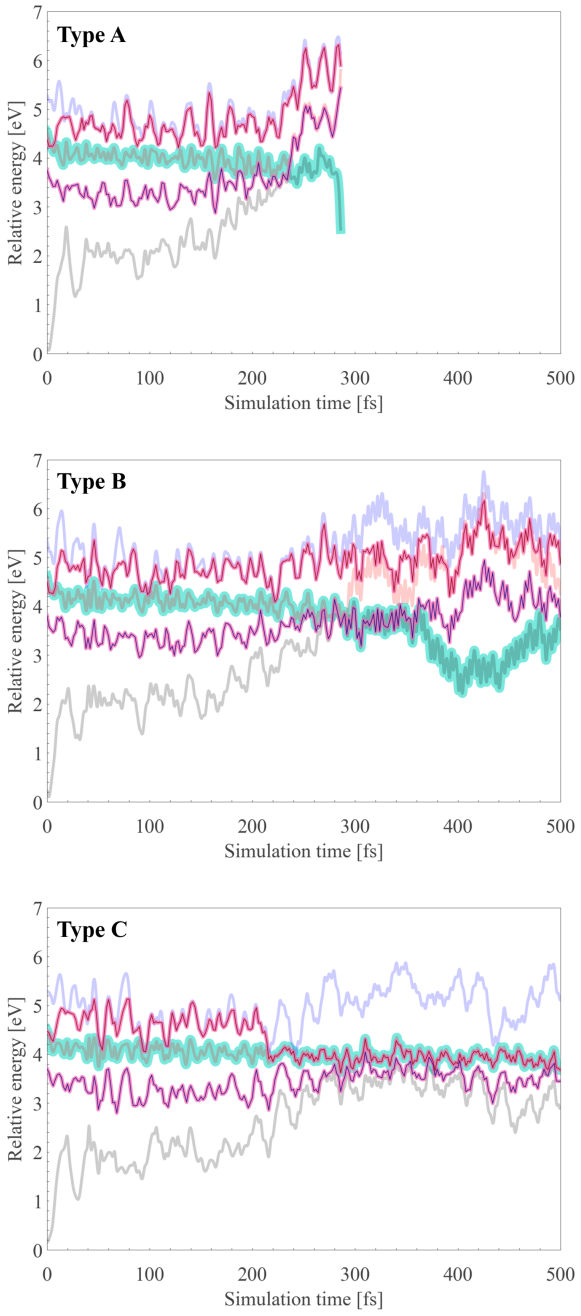

Figure 4.10. Three types of time evolution of triplet (T_1 and T_2) potential energies along given trajectories (top: Type A, middle: Type B, and bottom: Type C). Two lines covered with magenta represent the potential energies of triplet states. The line covered with sky blue represents the state where nuclei stay. For ease of viewing, the transparency of the line for each singlet state is increased.

4.4 Conclusion

With the development of experimental techniques, it has become possible to capture ultrafast excited state reactions in real time by time-resolved photoemission spectroscopy. On the other hand, it is not easy to interpret time-resolved spectra originated from complex excited-state reactions. Non-adiabatic molecular dynamics allows us to follow the excited state processes of molecules at the atomic level and play an important role in elucidating the origin of complex time-resolved photoelectron spectra. In the present study, we have simulated the excited-state intramolecular proton transfer (ESIPT) and the subsequent ground- and excited-state dynamics of *o*-NP by non-adiabatic molecular dynamics with MRSF-TDDFT method and Zhu-Nakamura global switching algorithm. MRSF-TDDFT overcomes the spin-contamination problem in the conventional SF-TDDFT method, applied to reaction path and non-adiabatic molecular dynamics calculations. For *o*-NP, MRSF-TDDFT qualitatively reproduces the reaction path from the Fanck-Condon point at CASPT2 level of theory [150], although MRSF-TDDFT overestimates the vertical excitation energies. Thus, non-adiabatic dynamics simulation by MRSF-TDDFT is expected to be in good agreement with the one by CASPT2, reducing a much computational cost. Zhu-Nakamura global switching algorithm evaluates a non-adiabatic transition probability based on the shape of the potential energy surfaces at a crossing point. This method does not require solving the Schrödinger equation along a classical trajectory as in Tully's Fewest switches algorithm, thus, the simulation is less expensive. This study achieves efficient nonadiabatic dynamics simulations using the MRSF-TDDFT and the Zhu-Nakamura global switching algorithm.

This study presents non-adiabatic molecular dynamics simulations on the ultrafast ESIPT and subsequent dynamics of *o*-NP before the photodissociation and new insights into

the complex spectra observed in previous studies. From the simulation, the ESIPT process completed fast within 40 fs, as previously expected, but the subsequent decay to the ground state with the HONO twist takes about 300 fs, longer than expected before. Only one-third of total classical trajectories relaxed to the ground state, and two dynamical pathways (type A and B) are obtained, one of which returns to *o*-NP and the other keeps the HONO form in the ratio of 1:2. Since two-thirds of the total classical trajectories (type C) stayed in the S_1 state for up to 500 fs and frequently intersected with the triplet state, it is considered that the HONO dissociation occurs after intersystem crossing to the triplet states in this dynamical pathway.

Finally, we note two issues to be addressed in future research. The first is to perform non-adiabatic molecular dynamics simulations that take into account the triplet state in order to fully understand the photodissociation reaction of o-NPs. A code to calculate spin-orbit coupling in MRSF-TDDFT has already been developed and will be available soon. Thus, this problem will be solved in the near future. And, although not done in this study, photoelectron spectrum simulations are needed for direct comparison with experimental data. Since several previous studies have addressed this issue as well, the methodology is publicly available, and the rest is a matter of technology.

Chapter V

General Conclusion

This thesis is devoted to exploring non-adiabatic molecular dynamics in terms of dependence on diabatic and adiabatic potential energy surfaces. In the present thesis, the following three issues were discussed.

In **Chapter 2**, the dependence of the SH-AIMD method on two types of potential energy surfaces (PESs) namely, the spin-pure (spin-diabatic) and spin-mixed (spin-adiabatic) potential energy surfaces, were discussed. Since the spin-pure and spin-mixed states are transformed into each other by a unitary transformation, the results should be the same if both nuclei and electrons are treated in a fully quantum manner. However, in the SH-AIMD method, nuclei are treated by the classical equation of motion and govern by a single one potential surface, thus the type of potential surface could affect the results. In this chapter, Tully's fewest switches (TFS) algorithm, which has been widely used to take state transitions into account, was employed. The time evolution of the electronic wavefunction is different between spin-pure and spin-mixed PES-based simulations for GeH_2 and later. The fractions of classical trajectories are similar for the SiH_2 and GeH_2 cases. On the other hand, for SnH_2 and PbH_2, the fractions of classical trajectories differ significantly between spin-pure

and spin-mixed PES-based simulations as well as the time evolution of the electronic wavefunction. In particular, in the case of PbH_2, about a half of the classical trajectories in the spin-pure PES-based simulation result in Pb + H_2 dissociation after unphysical transitions in large energy gap regions. This study specifically shows that the spin-mixed PES-based SH-AIMD simulation is required for systems with large spin-orbit couplings.

In **Chapter 3**, the SH-AIMD code with ZN global switching algorithm whose use has been growing recently was developed and applied to MH_2 systems. The TFS algorithm estimates the nonadiabatic transition probability based on the time-dependent electronic wave function along the classical trajectory and requires a non-adiabatic coupling vector for the time evolution of the electronic wavefunction, which increases the computational cost and limits the use of some electronic structure methods, while the ZN algorithm is superior in terms of computational cost and versatility because it uses only information on potential energy surfaces to estimate a non-adiabatic transition probability. In this chapter, as in Chapter 2, the dependence of the SH-AIMD method on spin-pure and spin-mixed potential energy surfaces was also discussed. The results of the ZN algorithm qualitatively reproduce those of the TFS algorithm, indicating that it is a method with a good balance between computational cost and accuracy.

In **Chapter 4**, the excited-state intramolecular proton transfer (ESIPT) and subsequent dynamics of *ortho*-nitrophenol (*o*-NP) are analyzed using the by non-adiabatic molecular dynamics based on the ZN algorithm. *o*-NP is a constituent molecule of the air pollutant PM2.5, and its photodissociation process has attracted attention as one of the important sources of nitrous acid (HONO) in atmospheric chemistry. The HONO formation was experimentally confirmed to occurs about 400 fs after excitation by femtosecond time-resolved photoemission spectroscopy. Previous experimental and theoretical studies have suggested that this dissociation process is preceded via an intersystem crossing to the triplet state. The

possibility of intersystem crossing was also demonstrated based on potential energy surfaces at the CASPT2 level. On the other hand, the detailed dynamical mechanism has not yet been clarified, such as the relaxation to the ground state that was expected to occurs after ESIPT. In this chapter, the SH-AIMD code developed based on the ZN algorithm, combined with the MRSF-TDDFT method, was successfully applied to the photo-reaction of *o*-NP, and then the dynamical mechanism of the ESIPT and subsequent branching processes is clarified.

In this thesis, I developed a SH-AIMD program capable of simulating both internal conversion and intersystem crossing in equal footing, followed by crosscutting and systematic validation of theory and method in non-adiabatic molecular dynamics and extension of algorithm and codes, with applications to excited-state reactions including photoreaction important in atmospheric chemistry. So far, simulations have been performed for molecular systems in the gas phase, but chemical reactions generally occur in the condensed phase. However, the non-adiabatic molecular dynamics study in the condensed phase is still not common due to the inevitable increase in computational cost, which should be addressed in future work.

Bibliography

[1] L. D. Landau, "Zur Theorie der Energieübertragung. II," *Physikalische Zeitschrift der Sowjetunion*, vol. 2, pp. 46–51, 1932.

[2] C. Zener, "Non-adiabatic crossing of energy levels," *Proceedings of the Royal Society of London. Series A, Containing Papers of a Mathematical and Physical Character*, vol. 137, pp. 696–702, 9 1932.

[3] E. Schrödinger, "An Undulatory Theory of the Mechanics of Atoms and Molecules," *Physical Review*, vol. 28, pp. 1049–1070, 12 1926.

[4] M. Born and K. Huang, *Dynamical theory of crystal lattices*. Oxford university press, 1996.

[5] M. Born and R. Oppenheimer, "Zur Quantentheorie der Molekeln," *Annalen der Physik*, vol. 389, pp. 457–484, 1 1927.

[6] H.-D. Meyer, U. Manthe, and L. S. Cederbaum, "The multi-configurational time-dependent hartree approach," *Chemical Physics Letters*, vol. 165, no. 1, pp. 73–78, 1990.

[7] M. H. Beck, A. Jäckle, G. A. Worth, and H.-D. Meyer, "The multiconfiguration time-dependent Hartree (MCTDH) method: a highly efficient algorithm for propagating wavepackets," *Physics Reports*, vol. 324, no. 1, pp. 1–105, 2000.

[8] H. Wang and M. Thoss, "Multilayer formulation of the multiconfiguration time-dependent Hartree theory," *The Journal of Chemical Physics*, vol. 119, no. 3, pp. 1289–1299, 2003.

[9] U. Manthe, "A multilayer multiconfigurational time-dependent Hartree approach for quantum dynamics on general potential energy surfaces," *The Journal of Chemical Physics*, vol. 128, no. 16, 2008.

[10] H. Wang, "Multilayer multiconfiguration time-dependent Hartree theory," *The Journal of Physical Chemistry A*, vol. 119, no. 29, pp. 7951–7965, 2015.

[11] A. Abedi, N. T. Maitra, and E. K. Gross, "Exact factorization of the time-dependent electron-nuclear wave function," *Physical Review Letters*, vol. 105, no. 12, p. 123002, 2010.

[12] A. Abedi, N. T. Maitra, and E. Gross, "Correlated electron-nuclear dynamics: Exact factorization of the molecular wavefunction," *The Journal of Chemical Physics*, vol. 137, no. 22, 2012.

[13] G. Worth, M. Robb, and I. Burghardt, "A novel algorithm for non-adiabatic direct dynamics using variational Gaussian wavepackets," *Faraday Discussions*, vol. 127, pp. 307–323, 2004.

[14] D. V. Shalashilin, "Quantum mechanics with the basis set guided by Ehrenfest trajectories: Theory and application to spin-boson model," *The Journal of Chemical Physics*, vol. 130, no. 24, 2009.

[15] D. V. Shalashilin, "Nonadiabatic dynamics with the help of multiconfigurational Ehrenfest method: Improved theory and fully quantum 24d simulation of pyrazine," *The Journal of Chemical Physics*, vol. 132, no. 24, 2010.

[16] T. J. Martinez, M. Ben-Nun, and R. Levine, "Multi-electronic-state molecular dynamics: A wave function approach with applications," *The Journal of Physical Chemistry*, vol. 100, no. 19, pp. 7884–7895, 1996.

[17] T. Martinez, M. Ben-Nun, and R. Levine, "Molecular collision dynamics on several electronic states," *The Journal of Physical Chemistry A*, vol. 101, no. 36, pp. 6389–6402, 1997.

[18] M. Ben-Nun and T. J. Martı´ nez, "Ab initio molecular dynamics study of cis–trans photoisomerization in ethylene," *Chemical Physics Letters*, vol. 298, no. 1-3, pp. 57–65, 1998.

[19] T. J. Martinez, "Insights for light-driven molecular devices from ab initio multiple spawning excited-state dynamics of organic and biological chromophores," *Accounts of Chemical Research*, vol. 39, no. 2, pp. 119–126, 2006.

[20] A. McLachlan, "A variational solution of the time-dependent schrodinger equation," *Molecular Physics*, vol. 8, no. 1, pp. 39–44, 1964.

[21] J. C. Tully and R. K. Preston, "Trajectory surface hopping approach to nonadiabatic molecular collisions: the reaction of H+ with D_2," *The Journal of Chemical Physics*, vol. 55, no. 2, pp. 562–572, 1971.

[22] J. C. Tully, "Molecular dynamics with electronic transitions," *The Journal of Chemical Physics*, vol. 93, pp. 1061–1071, 1990.

[23] A. Bjerre and E. Nikitin, "Energy transfer in collisions of an excited sodium atom with a nitrogen molecule," *Chemical Physics Letters*, vol. 1, no. 5, pp. 179–181, 1967.

[24] W. Chen, W. L. Hase, and H. Schlegel, "Ab initio classical trajectory study of H_2CO $\rightarrow$ H_2+CO dissociation," *Chemical Physics Letters*, vol. 228, pp. 436–442, 10 1994.

[25] T. Taketsugu and M. S. Gordon, "Dynamic Reaction Path Study of SiH_4 + H $^- \rightarrow$ SiH_5 $^-$ and the Berry Pseudorotation Mechanism," *The Journal of Physical Chemistry*, vol. 99, pp. 14597–14604, 10 1995.

[26] M. A. El-Sayed, "Spin—Orbit Coupling and the Radiationless Processes in Nitrogen Heterocyclics," *The Journal of Chemical Physics*, vol. 38, pp. 2834–2838, 6 1963.

[27] P. A. M. Dirac, "The quantum theory of the electron," *Proceedings of the Royal Society of London. Series A, Containing Papers of a Mathematical and Physical Character*, vol. 117, no. 778, pp. 610–624, 1928.

[28] P. A. M. Dirac, "The quantum theory of the electron. Part II," *Proceedings of the Royal Society of London. Series A, Containing Papers of a Mathematical and Physical Character*, vol. 118, no. 779, pp. 351–361, 1928.

[29] M. Douglas and N. M. Kroll, "Quantum electrodynamical corrections to the fine structure of helium," *Annals of Physics*, vol. 82, no. 1, pp. 89–155, 1974.

[30] B. A. Hess, "Applicability of the no-pair equation with free-particle projection operators to atomic and molecular structure calculations," *Physical Review A*, vol. 32, no. 2, p. 756, 1985.

[31] C. Chang, M. Pelissier, and P. Durand, "Regular two-component Pauli-like effective Hamiltonians in Dirac theory," *Physica Scripta*, vol. 34, no. 5, p. 394, 1986.

[32] T. Nakajima and K. Hirao, "A new relativistic theory: a relativistic scheme by eliminating small components (RESC)," *Chemical Physics Letters*, vol. 302, no. 5-6, pp. 383–391, 1999.

[33] J. Grotendorst, *Modern Methods and Algorithms of Quantum Chemistry*. NIC series, John von Neumann Institute for Computing (NIC), 2000.

[34] W. Kutzelnigg and W. Liu, "Quasirelativistic theory equivalent to fully relativistic theory," *The Journal of Chemical Physics*, vol. 123, no. 24, 2005.

[35] H. A. Bethe and E. E. Salpeter, *Quantum mechanics of one-and two-electron atoms*. Springer Science & Business Media, 2012.

[36] V. Fock, "Näherungsmethode zur Lösung des quantenmechanischen Mehrkörperproblems," *Zeitschrift für Physik*, vol. 61, pp. 126–148, 1930.

[37] J. C. Slater, "Note on Hartree's method," *Physical Review*, vol. 35, no. 2, p. 210, 1930.

[38] F. Coester, "Bound states of a many-particle system," *Nuclear Physics*, vol. 7, pp. 421–424, 1958.

[39] K. Raghavachari, G. W. Trucks, J. A. Pople, and M. Head-Gordon, "A fifth-order perturbation comparison of electron correlation theories," *Chemical Physics Letters*, vol. 157, no. 6, pp. 479–483, 1989.

[40] H. Sekino and R. J. Bartlett, "A linear response, coupled-cluster theory for excitation energy," *International Journal of Quantum Chemistry*, vol. 26, no. S18, pp. 255–265, 1984.

[41] J. F. Stanton and R. J. Bartlett, "The equation of motion coupled-cluster method. A systematic biorthogonal approach to molecular excitation energies, transition probabilities, and excited state properties," *The Journal of Chemical Physics*, vol. 98, no. 9, pp. 7029–7039, 1993.

[42] N. Nakatsuji, "Cluster expansion of the wavefunction. Excited states," *Chemical Physics Letters*, vol. 59, no. 2, pp. 362–364, 1978.

[43] H. Nakatsuji and K. Hirao, "Cluster expansion of the wavefunction. Symmetry-adapted-cluster expansion, its variational determination, and extension of open-shell orbital theory," *The Journal of Chemical Physics*, vol. 68, no. 5, pp. 2053–2065, 1978.

[44] H. Nakatsuji, "Cluster expansion of the wavefunction. electron correlations in ground and excited states by sac (symmetry-adapted-cluster) and sac ci theories," *Chemical Physics Letters*, vol. 67, no. 2-3, pp. 329–333, 1979.

[45] H. J. Monkhorst, "Calculation of properties with the coupled-cluster method," *International Journal of Quantum Chemistry*, vol. 12, no. S11, pp. 421–432, 1977.

[46] E. Dalgaard and H. J. Monkhorst, "Some aspects of the time-dependent coupled-cluster approach to dynamic response functions," *Physical Review A*, vol. 28, no. 3, p. 1217, 1983.

[47] C. Møller and M. S. Plesset, "Note on an approximation treatment for many-electron systems," *Physical Review*, vol. 46, no. 7, p. 618, 1934.

[48] J. Frenkel, *Wave mechanics, advanced general theory*, vol. 436. Oxford, 1934.

[49] H. Werner and P. J. Knowles, "A second order multiconfiguration SCF procedure with optimum convergence," *The Journal of Chemical Physics*, vol. 82, pp. 5053–5063, 6 1985.

[50] P. J. Knowles and H.-J. Werner, "An efficient second-order MC SCF method for long configuration expansions," *Chemical Physics Letters*, vol. 115, pp. 259–267, 4 1985.

[51] J. Olsen, B. O. Roos, P. Jørgensen, and H. J. A. Jensen, "Determinant based configuration interaction algorithms for complete and restricted configuration interaction spaces," *The Journal of Chemical Physics*, vol. 89, no. 4, pp. 2185–2192, 1988.

[52] A. Banerjee and J. Simons, "The coupled-cluster method with a multiconfiguration reference state," *International Journal of Quantum Chemistry*, vol. 19, no. 2, pp. 207–216, 1981.

[53] N. Oliphant and L. Adamowicz, "The implementation of the multireference coupled-cluster method based on the single-reference formalism," *The Journal of chemical physics*, vol. 96, no. 5, pp. 3739–3744, 1992.

[54] M. Kállay, P. R. Nagy, D. Mester, Z. Rolik, G. Samu, J. Csontos, J. Csóka, P. B. Szabó, L. Gyevi-Nagy, B. Hégely, *et al.*, "The MRCC program system: Accurate quantum

chemistry from water to proteins," *The Journal of chemical physics*, vol. 152, no. 7, 2020.

[55] K. Andersson, P. A. Malmqvist, B. O. Roos, A. J. Sadlej, and K. Wolinski, "Second-order perturbation theory with a CASSCF reference function," *Journal of Physical Chemistry*, vol. 94, no. 14, pp. 5483–5488, 1990.

[56] K. Andersson, P.-Å. Malmqvist, and B. O. Roos, "Second-order perturbation theory with a complete active space self-consistent field reference function," *The Journal of Chemical Physics*, vol. 96, no. 2, pp. 1218–1226, 1992.

[57] J. Finley, P.-Å. Malmqvist, B. O. Roos, and L. Serrano-Andrés, "The multi-state CASPT2 method," *Chemical physics letters*, vol. 288, no. 2-4, pp. 299–306, 1998.

[58] T. Shiozaki, W. Győrffy, P. Celani, and H.-J. Werner, "Communication: Extended multi-state complete active space second-order perturbation theory: Energy and nuclear gradients," *The Journal of Chemical Physics*, vol. 135, no. 8, 2011.

[59] S. Battaglia and R. Lindh, "Extended dynamically weighted CASPT2: The best of two worlds," *Journal of chemical theory and computation*, vol. 16, no. 3, pp. 1555–1567, 2020.

[60] Y. Nishimoto, S. Battaglia, and R. Lindh, "Analytic First-Order Derivatives of (X)MS, XDW, and RMS Variants of the CASPT2 and RASPT2 methods," *Journal of Chemical Theory and Computation*, vol. 18, pp. 4269–4281, 7 2022.

[61] K. Hirao, "Multireference Møller—Plesset method," *Chemical physics letters*, vol. 190, no. 3-4, pp. 374–380, 1992.

[62] H. Nakano, "Quasidegenerate perturbation theory with multiconfigurational self-consistent-field reference functions," *The Journal of Chemical Physics*, vol. 99, no. 10, pp. 7983–7992, 1993.

[63] A. A. Granovsky, "Extended multi-configuration quasi-degenerate perturbation theory: The new approach to multi-state multi-reference perturbation theory," *The Journal of Chemical Physics*, vol. 134, no. 21, 2011.

[64] C. Angeli, R. Cimiraglia, S. Evangelisti, T. Leininger, and J.-P. Malrieu, "Introduction of *n*-electron valence states for multireference perturbation theory," *The Journal of Chemical Physics*, vol. 114, no. 23, pp. 10252–10264, 2001.

[65] C. Angeli, S. Borini, M. Cestari, and R. Cimiraglia, "A quasidegenerate formulation of the second order *n*-electron valence state perturbation theory approach," *The Journal of Chemical Physics*, vol. 121, no. 9, pp. 4043–4049, 2004.

[66] W. Kohn and L. J. Sham, "Self-consistent equations including exchange and correlation effects," *Physical Review*, vol. 140, no. 4A, p. A1133, 1965.

[67] A. D. Becke, "Density-functional exchange-energy approximation with correct asymptotic behavior," *Physical Review A*, vol. 38, no. 6, p. 3098, 1988.

[68] C. Lee, W. Yang, and R. G. Parr, "Development of the Colle-Salvetti correlation-energy formula into a functional of the electron density," *Physical Review B*, vol. 37, no. 2, p. 785, 1988.

[69] P. Hohenberg and W. Kohn, "Inhomogeneous electron gas," *Physical Review*, vol. 136, no. 3B, p. B864, 1964.

[70] W. Kutzelnigg, "Density functional theory in terms of a Legendre transformation for beginners," *Journal of Molecular Structure: THEOCHEM*, vol. 768, no. 1-3, pp. 163–173, 2006.

[71] J. P. Perdew, K. Burke, and M. Ernzerhof, "Generalized gradient approximation made simple," *Physical review letters*, vol. 77, no. 18, p. 3865, 1996.

[72] S. Grimme, J. G. Brandenburg, C. Bannwarth, and A. Hansen, "Consistent structures and interactions by density functional theory with small atomic orbital basis sets," *The Journal of chemical physics*, vol. 143, no. 5, 2015.

[73] R. Nagai, R. Akashi, and O. Sugino, "Completing density functional theory by machine learning hidden messages from molecules," *npj Computational Materials*, vol. 6, no. 1, p. 43, 2020.

[74] E. Runge and E. K. Gross, "Density-functional theory for time-dependent systems," *Physical Review Letters*, vol. 52, no. 12, p. 997, 1984.

[75] M. A. Marques and M. Marques, *Time-dependent density functional theory*, vol. 706. Springer Science & Business Media, 2006.

[76] Y. Shao, M. Head-Gordon, and A. I. Krylov, "The spin–flip approach within time-dependent density functional theory: Theory and applications to diradicals," *The Journal of Chemical Physics*, vol. 118, no. 11, pp. 4807–4818, 2003.

[77] D. Casanova and A. I. Krylov, "Spin-flip methods in quantum chemistry," *Physical Chemistry Chemical Physics*, vol. 22, no. 8, pp. 4326–4342, 2020.

[78] Y. Harabuchi, S. Maeda, T. Taketsugu, N. Minezawa, and K. Morokuma, "Automated search for minimum energy conical intersection geometries between the lowest two

singlet states S_0/S_1-MECIs by the spin-flip TDDFT method," *Journal of Chemical Theory and Computation*, vol. 9, no. 9, pp. 4116–4123, 2013.

[79] Y. Harabuchi, K. Keipert, F. Zahariev, T. Taketsugu, and M. S. Gordon, "Dynamics simulations with spin-flip time-dependent density functional theory: Photoisomerization and photocyclization mechanisms of cis-stilbene in $\pi\pi^*$ states," *The Journal of Physical Chemistry A*, vol. 118, no. 51, pp. 11987–11998, 2014.

[80] S. Lee, M. Filatov, S. Lee, and C. H. Choi, "Eliminating spin-contamination of spin-flip time dependent density functional theory within linear response formalism by the use of zeroth-order mixed-reference (MR) reduced density matrix," *The Journal of Chemical Physics*, vol. 149, no. 10, 2018.

[81] S. Lee, E. E. Kim, H. Nakata, S. Lee, and C. H. Choi, "Efficient implementations of analytic energy gradient for mixed-reference spin-flip time-dependent density functional theory (MRSF-TDDFT)," *The Journal of Chemical Physics*, vol. 150, no. 18, 2019.

[82] J. W. Park and T. Shiozaki, "On-the-Fly CASPT2 Surface-Hopping Dynamics," *Journal of Chemical Theory and Computation*, vol. 13, pp. 3676–3683, 8 2017.

[83] W. Park, S. Lee, M. Huix-Rotllant, M. Filatov, and C. H. Choi, "Impact of the dynamic electron correlation on the unusually long excited-state lifetime of thymine," *The Journal of Physical Chemistry Letters*, vol. 12, no. 18, pp. 4339–4346, 2021.

[84] S. Shostak, W. Park, J. Oh, J. Kim, S. Lee, H. Nam, M. Filatov, D. Kim, and C. H. Choi, "Ultrafast excited state aromatization in dihydroazulene," *Journal of the American Chemical Society*, vol. 145, no. 3, pp. 1638–1648, 2023.

[85] M. Huix-Rotllant, K. Schwinn, V. Pomogaev, M. Farmani, N. Ferré, S. Lee, and C. H. Choi, "Photochemistry of thymine in solution and dna revealed by an electrostatic embedding qm/mm combined with mixed-reference spin-flip tddft," *Journal of Chemical Theory and Computation*, vol. 19, no. 1, pp. 147–156, 2022.

[86] T. Taketsugu, A. Tajima, K. Ishii, and T. Hirano, "Ab Initio Direct Trajectory Simulation with Nonadiabatic Transitions of the Dissociative Recombination Reaction $HCNH^+ + e^- \rightarrow HNC/HCN + H$," *The Astrophysical Journal*, vol. 608, pp. 323–329, 6 2004.

[87] T. Kobayashi, M. Shiga, A. Murakami, and S. Nakamura, "Ab initio Study of Ultrafast Photochemical Reaction Dynamics of Phenol Blue," *Journal of the American Chemical Society*, vol. 129, pp. 6405–6424, 5 2007.

[88] Y. Ootani, K. Satoh, A. Nakayama, T. Noro, and T. Taketsugu, "Ab initio molecular dynamics simulation of photoisomerization in azobenzene in the $n\pi^*$ state," *The Journal of Chemical Physics*, vol. 131, p. 194306, 2009.

[89] A. Nakayama, G. Arai, S. Yamazaki, and T. Taketsugu, "Solvent effects on the ultrafast nonradiative deactivation mechanisms of thymine in aqueous solution: Excited-state QM/MM molecular dynamics simulations," *The Journal of Chemical Physics*, vol. 139, p. 214304, 12 2013.

[90] R. Borrego-Varillas, A. Nenov, P. Kabaciński, I. Conti, L. Ganzer, A. Oriana, V. K. Jaiswal, I. Delfino, O. Weingart, C. Manzoni, I. Rivalta, M. Garavelli, and G. Cerullo, "Tracking excited state decay mechanisms of pyrimidine nucleosides in real time," *Nature Communications*, vol. 12, p. 7285, 12 2021.

[91] S. Hammes ‐ Schiffer and J. C. Tully, "Proton transfer in solution: Molecular dynamics with quantum transitions," *The Journal of Chemical Physics*, vol. 101, pp. 4657–4667, 9 1994.

[92] F. Plasser, M. Ruckenbauer, S. Mai, M. Oppel, P. Marquetand, and L. González, "Efficient and Flexible Computation of Many-Electron Wave Function Overlaps," *Journal of Chemical Theory and Computation*, vol. 12, pp. 1207–1219, 2016.

[93] M. Dallos, H. Lischka, R. Shepard, D. R. Yarkony, and P. G. Szalay, "Analytic evaluation of nonadiabatic coupling terms at the MR-CI level. II. Minima on the crossing seam: Formaldehyde and the photodimerization of ethylene," *The Journal of Chemical Physics*, vol. 120, pp. 7330–7339, 4 2004.

[94] I. Tavernelli, B. F. Curchod, A. Laktionov, and U. Rothlisberger, "Nonadiabatic coupling vectors for excited states within time-dependent density functional theory in the Tamm-Dancoff approximation and beyond," *Journal of Chemical Physics*, vol. 133, 2010.

[95] T. Mori, W. J. Glover, M. S. Schuurman, and T. J. Martinez, "Role of Rydberg States in the Photochemical Dynamics of Ethylene," *The Journal of Physical Chemistry A*, vol. 116, pp. 2808–2818, 3 2012.

[96] J. W. Park and T. Shiozaki, "Analytical Derivative Coupling for Multistate CASPT2 Theory," *Journal of Chemical Theory and Computation*, vol. 13, pp. 2561–2570, 6 2017.

[97] M. Heindl and L. González, "A XMS-CASPT2 non-adiabatic dynamics study on pyrrole," *Computational and Theoretical Chemistry*, vol. 1155, pp. 38–46, 5 2019.

[98] N. Minezawa and T. Nakajima, "Trajectory surface hopping molecular dynamics simulation by spin-flip time-dependent density functional theory," *The Journal of Chemical Physics*, vol. 150, p. 204120, 5 2019.

[99] P. Chakraborty, Y. Liu, T. Weinacht, and S. Matsika, "Effect of dynamic correlation on the ultrafast relaxation of uracil in the gas phase," *Faraday Discussions*, vol. 228, pp. 266–285, 2021.

[100] N. Bellonzi, G. R. Medders, E. Epifanovsky, and J. E. Subotnik, "Configuration interaction singles with spin-orbit coupling: Constructing spin-adiabatic states and their analytical nuclear gradients," *The Journal of Chemical Physics*, vol. 150, p. 014106, 1 2019.

[101] N. Bellonzi, E. Alguire, S. Fatehi, Y. Shao, and J. E. Subotnik, "TD-DFT spin-adiabats with analytic nonadiabatic derivative couplings," *The Journal of Chemical Physics*, vol. 152, p. 044112, 1 2020.

[102] L. T. Belcher, C. D. Lewis, G. S. Kedziora, and D. E. Weeks, "Analytic non-adiabatic derivative coupling terms for spin-orbit MRCI wavefunctions. II. Derivative coupling terms and coupling angle for KHe($A_2\ \pi_{1/2}$) $\Leftrightarrow$ KHe($B_2\ \sigma_{1/2}$)," *The Journal of Chemical Physics*, vol. 151, p. 234109, 12 2019.

[103] M. Kamiya and T. Taketsugu, "Ab initio surface hopping excited ‐ state molecular dynamics approach on the basis of spin − orbit coupled states: An application to the A ‐ band photodissociation of Ch_3i," *Journal of Computational Chemistry*, vol. 40, pp. 456–463, 1 2019.

[104] M. Richter, P. Marquetand, J. González-Vázquez, I. Sola, and L. González, "SHARC: ab Initio Molecular Dynamics with Surface Hopping in the Adiabatic Representation Including Arbitrary Couplings," *Journal of Chemical Theory and Computation*, vol. 7, pp. 1253–1258, 5 2011.

[105] S. Mai, P. Marquetand, and L. González, "Nonadiabatic dynamics: The SHARC approach," *WIREs Computational Molecular Science*, vol. 8, 11 2018.

[106] C. E. Crespo-Hernández, L. Martínez-Fernández, C. Rauer, C. Reichardt, S. Mai, M. Pollum, P. Marquetand, L. González, and I. Corral, "Electronic and Structural Elements That Regulate the Excited-State Dynamics in Purine Nucleobase Derivatives," *Journal of the American Chemical Society*, vol. 137, pp. 4368–4381, 2015.

[107] J. P. Zobel, J. J. Nogueira, and L. González, "Mechanism of Ultrafast Intersystem Crossing in 2-Nitronaphthalene," *Chemistry - A European Journal*, vol. 24, pp. 5379–5387, 2018.

[108] C. Carbogno, J. Behler, A. Groß, and K. Reuter, "Fingerprints for Spin-Selection Rules in the Interaction Dynamics of O_2 at Al(111)," *Physical Review Letters*, vol. 101, p. 096104, 8 2008.

[109] G. Cui and W. Thiel, "Generalized trajectory surface-hopping method for internal conversion and intersystem crossing," *The Journal of Chemical Physics*, vol. 141, p. 124101, 9 2014.

[110] F. F. de Carvalho and I. Tavernelli, "Nonadiabatic dynamics with intersystem crossings: A time-dependent density functional theory implementation," *The Journal of Chemical Physics*, vol. 143, p. 224105, 12 2015.

[111] B.-B. Xie, B.-L. Liu, X.-F. Tang, D. Tang, L. Shen, and W.-H. Fang, "Nonadiabatic dynamics simulation of photoinduced ring-opening reaction of 2(5*H*)-thiophenone with internal conversion and intersystem crossing," *Physical Chemistry Chemical Physics*, vol. 23, pp. 9867–9877, 2021.

[112] G. Granucci, M. Persico, and G. Spighi, "Surface hopping trajectory simulations with spin-orbit and dynamical couplings," *The Journal of Chemical Physics*, vol. 137, p. 22A501, 12 2012.

[113] J. Peng, Y. Xie, D. Hu, and Z. Lan, "Performance of trajectory surface hopping method in the treatment of ultrafast intersystem crossing dynamics," *The Journal of Chemical Physics*, vol. 150, p. 164126, 4 2019.

[114] N. Matsunaga, S. Koseki, and M. S. Gordon, "Relativistic potential energy surfaces of XH_2 (X= C, Si, Ge, Sn, and Pb) molecules: Coupling of $^1A_1$ and $^3B_1$ states," *The Journal of Chemical Physics*, vol. 104, no. 20, pp. 7988–7996, 1996.

[115] A. BERNING, M. SCHWEIZER, H.-J. WERNER, P. J. KNOWLES, and P. PALMIERI, "Spin-orbit matrix elements for internally contracted multireference configuration interaction wavefunctions," *Molecular Physics*, vol. 98, pp. 1823–1833, 11 2000.

[116] T. H. Dunning, "Gaussian basis sets for use in correlated molecular calculations. I. The atoms boron through neon and hydrogen," *The Journal of Chemical Physics*, vol. 90, pp. 1007–1023, 1 1989.

[117] D. E. Woon and T. H. Dunning, "Gaussian basis sets for use in correlated molecular calculations. III. The atoms aluminum through argon," *The Journal of Chemical Physics*, vol. 98, pp. 1358–1371, 1 1993.

[118] K. A. Peterson, "Systematically convergent basis sets with relativistic pseudopotentials. I. Correlation consistent basis sets for the post- d group 13 – 15 elements," *The Journal of Chemical Physics*, vol. 119, pp. 11099–11112, 12 2003.

[119] H. J. Werner, P. J. Knowles, G. Knizia, F. R. Manby, and M. Schütz, "Molpro: A general-purpose quantum chemistry program package," *Wiley Interdisciplinary Reviews: Computational Molecular Science*, vol. 2, pp. 242–253, 2012.

[120] H.-J. Werner, P. J. Knowles, G. Knizia, F. R. Manby, M. Schutz, P. Celani, T. Korona, R. Lindh, A. Mitrushenkov, G. Rauhut, K. R. Shamasundar, T. B. Adler, R. D. Amos, A. Bernhardsson, A. Berning, D. L. Cooper, M. J. O. Deegan, A. J. Dobbyn, F. Eckert, E. Goll, C. Hampel, A. Hesselmann, G. Hetzer, T. Hrenar, G. Jansen, C. Koppl, Y. Liu, A. W. Lloyd, R. A. Mata, A. J. May, S. J. McNicholas, W. Meyer, M. E. Mura, A. Nicklass, D. P. O' Neill, P. Palmieri, D. Peng, K. Pfluger, R. Pitzer, M. Reiher, T. Shiozaki, H. Stoll, A. J. Stone, R. Tarroni, T. Thorsteinsson, and M. Wang, "MOLPRO, version 2012.1, a package of ab initio programs," 2012.

[121] S. Maeda, K. Ohno, and K. Morokuma, "Systematic exploration of the mechanism of chemical reactions: the global reaction route mapping (GRRM) strategy using the ADDF and AFIR methods," *Physical Chemistry Chemical Physics*, vol. 15, p. 3683, 2013.

[122] S. Maeda, Y. Harabuchi, Y. Sumiya, M. Takagi, K. Suzuki, M. Hatanaka, Y. Osada, T. Taketsugu, K. Morokuma, and K. Ohno, "GRRM17."

[123] R. R. Zaari and S. A. Varganov, "Nonadiabatic Transition State Theory and Trajectory Surface Hopping Dynamics: Intersystem Crossing Between $^3B_1$ and $^1A_1$ States of SiH_2," *The Journal of Physical Chemistry A*, vol. 119, pp. 1332–1338, 2 2015.

[124] D. A. Fedorov, S. R. Pruitt, K. Keipert, M. S. Gordon, and S. A. Varganov, "Ab Initio Multiple Spawning Method for Intersystem Crossing Dynamics: Spin-Forbidden Transitions between $^3B_1$ and $^1A_1$ States of GeH_2," *The Journal of Physical Chemistry A*, vol. 120, pp. 2911–2919, 5 2016.

[125] T. Ishida, S. Nanbu, and H. Nakamura, "Nonadiabatic ab initio Dynamics of Two Models of Schiff Base Retinal," *The Journal of Physical Chemistry A*, vol. 113, pp. 4356–4366, 4 2009.

[126] L. Yu, C. Xu, Y. Lei, C. Zhu, and Z. Wen, "Trajectory-based nonadiabatic molecular dynamics without calculating nonadiabatic coupling in the avoided crossing case: trans ↔ cis photoisomerization in azobenzene," *Physical Chemistry Chemical Physics*, vol. 16, pp. 25883–25895, 2014.

[127] A. Ohta, O. Kobayashi, S. O. Danielache, and S. Nanbu, "Nonadiabatic ab initio molecular dynamics with PME-ONIOM scheme of photoisomerization reaction between 1,3-cyclohexadiene and 1,3,5-cis-hexatriene in solution phase," *Chemical Physics*, vol. 485-486, pp. 45–59, 3 2017.

[128] C. Xu, L. Yu, C. Zhu, J. Yu, and Z. Cao, "Intersystem crossing-branched excited-state intramolecular proton transfer for *o*-nitrophenol: An ab initio on-the-fly nonadiabatic molecular dynamic simulation," *Scientific Reports*, vol. 6, p. 26768, 5 2016.

[129] C. Xu, F. L. Gu, and C. Zhu, "Ultrafast intersystem crossing for nitrophenols:: Ab initio nonadiabatic molecular dynamics simulation," *Physical Chemistry Chemical Physics*, vol. 20, pp. 5606–5616, 2018.

[130] L. Yue, L. Yu, C. Xu, C. Zhu, and Y. Liu, "Quantum yields of singlet and triplet chemiexcitation of dimethyl 1,2-dioxetane: Ab initio nonadiabatic molecular dynamic simulations," *Physical Chemistry Chemical Physics*, vol. 22, pp. 11440–11451, 2020.

[131] K. Hanasaki, M. Kanno, T. A. Niehaus, and H. Kono, "An efficient approximate algorithm for nonadiabatic molecular dynamics," *The Journal of Chemical Physics*, vol. 149, p. 244117, 12 2018.

[132] C. Zhu and H. Nakamura, "Theory of nonadiabatic transition for general two-state curve crossing problems. I. Nonadiabatic tunneling case," *The Journal of Chemical Physics*, vol. 101, no. 12, pp. 10630–10647, 1994.

[133] C. Zhu and H. Nakamura, "Theory of nonadiabatic transition for general two-state curve crossing problems. II. Landau–Zener case," *The Journal of Chemical Physics*, vol. 102, no. 19, pp. 7448–7461, 1995.

[134] L. Yue, L. Yu, C. Xu, Y. Lei, Y. Liu, and C. Zhu, "Benchmark performance of global switching versus local switching for trajectory surface hopping molecular dynamics simulation: cis $\leftrightarrow$ trans azobenzene photoisomerization," *ChemPhysChem*, vol. 18, no. 10, pp. 1274–1287, 2017.

[135] Y.-Q. Wang, H.-G. Wang, S.-Q. Zhang, K.-M. Pei, X. Zheng, and D. Lee Phillips, "Resonance Raman intensity analysis of the excited state proton transfer dynamics

of 2-nitrophenol in the charge-transfer band absorption," *The Journal of Chemical Physics*, vol. 125, no. 21, 2006.

[136] K. K. Namboodiri, S. Viswanathan, R. Ganesan, and V. J. Bhasu, "The electronic structure, spectra, and reactivity of nitrophenols," *Journal of Computational Chemistry*, vol. 2, no. 4, pp. 392–401, 1981.

[137] G. Woolfe, M. Melzig, S. Schneider, and F. Dörr, "The role of tautomeric and rotameric species in the photophysics of 2-(2′ -hydroxyphenyl) benzoxazole," *Chemical Physics*, vol. 77, no. 2, pp. 213–221, 1983.

[138] C. Leuenberger, M. P. Ligocki, and J. F. Pankow, "Trace organic compounds in rain. 4. Identities, concentrations, and scavenging mechanisms for phenols in urban air and rain," *Environmental Science & Technology*, vol. 19, no. 11, pp. 1053–1058, 1985.

[139] M. A. Harrison, S. Barra, D. Borghesi, D. Vione, C. Arsene, and R. I. Olariu, "Nitrated phenols in the atmosphere: a review," *Atmospheric Environment*, vol. 39, no. 2, pp. 231–248, 2005.

[140] I. Bejan, Y. Abd El Aal, I. Barnes, T. Benter, B. Bohn, P. Wiesen, and J. Kleffmann, "The photolysis of *ortho*-nitrophenols: a new gas phase source of HONO," *Physical Chemistry Chemical Physics*, vol. 8, no. 17, pp. 2028–2035, 2006.

[141] M. Sangwan and L. Zhu, "Absorption cross sections of 2-nitrophenol in the 295–400 nm region and photolysis of 2-nitrophenol at 308 and 351 nm," *The Journal of Physical Chemistry A*, vol. 120, no. 50, pp. 9958–9967, 2016.

[142] R. M. Harrison, J. D. Peak, and G. M. Collins, "Tropospheric cycle of nitrous acid," *Journal of Geophysical Research: Atmospheres*, vol. 101, no. D9, pp. 14429–14439, 1996.

[143] Q. Wei, H.-M. Yin, J.-L. Sun, X.-F. Yue, and K.-L. Han, "The dynamics of OH channel in the 266 and 355 nm photodissociation of 2-nitrophenol," *Chemical Physics Letters*, vol. 463, no. 4-6, pp. 340–344, 2008.

[144] M. Takezaki, N. Hirota, and M. Terazima, "Nonradiative relaxation processes and electronically excited states of nitrobenzene studied by picosecond time-resolved transient grating method," *The Journal of Physical Chemistry A*, vol. 101, no. 19, pp. 3443–3448, 1997.

[145] S.-B. Cheng, C.-H. Zhou, H.-M. Yin, J.-L. Sun, and K.-L. Han, "OH produced from *o*-nitrophenol photolysis: A combined experimental and theoretical investigation," *The Journal of Chemical Physics*, vol. 130, no. 23, 2009.

[146] L. Vereecken, H. Chakravarty, B. Bohn, and J. Lelieveld, "Theoretical study on the formation of H-and O-atoms, HONO, OH, NO, and NO_2 from the lowest lying singlet and triplet states in *ortho*-nitrophenol photolysis," *International Journal of Chemical Kinetics*, vol. 48, no. 12, pp. 785–795, 2016.

[147] H. A. Ernst, T. J. Wolf, O. Schalk, N. González-García, A. E. Boguslavskiy, A. Stolow, M. Olzmann, and A.-N. Unterreiner, "Ultrafast dynamics of *o*-nitrophenol: An experimental and theoretical study," *The Journal of Physical Chemistry A*, vol. 119, no. 35, pp. 9225–9235, 2015.

[148] C. Xu, L. Yu, C. Zhu, and J. Yu, "Photoisomerization reaction mechanisms of *o*-nitrophenol revealed by analyzing intersystem crossing network at the MRCI level," *The Journal of Physical Chemistry A*, vol. 119, no. 42, pp. 10441–10450, 2015.

[149] A. Ciavardini, M. Coreno, C. Callegari, C. Spezzani, G. De Ninno, B. Ressel, C. Grazioli, M. de Simone, A. Kivimaki, P. Miotti, *et al.*, "Ultra-fast-VUV photoemission study of UV excited 2-nitrophenol," *The Journal of Physical Chemistry A*, vol. 123, no. 7, pp. 1295–1302, 2019.

[150] Y. Nitta, O. Schalk, H. Igarashi, S. Wada, T. Tsutsumi, K. Saita, T. Taketsugu, and T. Sekikawa, "Real-time probing of an atmospheric photochemical reaction by ultrashort extreme ultraviolet pulses: Nitrous acid release from o-nitrophenol," *The Journal of Physical Chemistry Letters*, vol. 12, no. 1, pp. 674–679, 2021.

[151] S. McClung, D. Abeygunewardane, S. Matsika, and T. Weinacht, "Excited-state dynamics of o-nitrophenol studied with UV pump–VUV probe time-resolved photoelectron and photoion spectroscopy," *The Journal of Chemical Physics*, vol. 158, no. 14, 2023.

[152] S. Bailey-Darland, T. D. Krueger, and C. Fang, "Ultrafast spectroscopies of nitrophenols and nitrophenolates in solution: From electronic dynamics and vibrational structures to photochemical and environmental implications," *Molecules*, vol. 28, no. 2, p. 601, 2023.

[153] S. Guo and H. Li, "Photolysis of nitrophenols in gas phase and aqueous environment: a potential daytime source for atmospheric nitrous acid (HONO)," *Environmental Science: Atmospheres*, vol. 3, no. 1, pp. 143–155, 2023.

[154] M. J. Frisch, G. W. Trucks, H. B. Schlegel, G. E. Scuseria, M. A. Robb, J. R. Cheeseman, G. Scalmani, V. Barone, G. A. Petersson, H. Nakatsuji, X. Li, M. Caricato, A. V. Marenich, J. Bloino, B. G. Janesko, R. Gomperts, B. Mennucci, H. P. Hratchian, J. V. Ortiz, A. F. Izmaylov, J. L. Sonnenberg, D. Williams-Young, F. Ding, F. Lipparini, F. Egidi, J. Goings, B. Peng, A. Petrone, T. Henderson, D. Ranasinghe, V. G. Zakrzewski, J. Gao, N. Rega, G. Zheng, W. Liang, M. Hada, M. Ehara, K. Toyota, R. Fukuda, J. Hasegawa, M. Ishida, T. Nakajima, Y. Honda, O. Kitao, H. Nakai, T. Vreven, K. Throssell, J. A. Montgomery, Jr., J. E. Peralta, F. Ogliaro, M. J. Bearpark, J. J. Heyd, E. N. Brothers, K. N. Kudin, V. N. Staroverov, T. A. Keith, R. Kobayashi, J. Normand, K. Raghavachari, A. P. Rendell, J. C. Burant, S. S. Iyengar, J. Tomasi, M. Cossi, J. M. Millam, M. Klene, C. Adamo, R. Cammi, J. W. Ochterski, R. L. Martin, K. Morokuma, O. Farkas, J. B. Foresman, and D. J. Fox, "Gaussian 16 Revision C.01," 2016. Gaussian Inc. Wallingford CT.

[155] G. M. Barca, C. Bertoni, L. Carrington, D. Datta, N. DeSilva, E. J. Deustua, D. Fedorov, J. R. Gour, A. O. Gunina, E. Guidez, T. Harville, S. Irle, J. Ivanic, K. Kowalski, S. Leang, H. Li, W. Li, J. Lutz, I. Magoulas, J. Mato, V. Mirionov, H. Nakata, B. Q. Pham, P. Piecuch, D. Poole, S. Pruitt, A. P. Rendell, L. B. Roskop, K. Ruedenberg, T. Sattasathuchana, M. W. Schmidt, J. Shen, L. Slipchenko, M. Sosonkina, V. Sundriyal, A. Tiwari, J. L. Galvez Vallejo, B. Westheimer, M. W. Wloch, P. Xu, F. Zahariev, and M. S. Gordon, "Recent developments in the general atomic and molecular electronic structure system," *Journal of Chemical Physics*, vol. 152, 4 2020.

[156] G. Li Manni, I. Fdez. Galván, A. Alavi, F. Aleotti, F. Aquilante, J. Autschbach, D. Avagliano, A. Baiardi, J. Bao, S. Battaglia, L. Birnoschi, A. Blanco-González, S. Bokarev, R. Broer, R. Cacciari, P. Calio, R. Carlson, R. Carvalho Couto, L. Cerdán,

L. Chibotaru, N. Chilton, J. Church, I. Conti, S. Coriani, J. Cuéllar-Zuquin, R. Daoud, N. Dattani, P. Decleva, C. de Graaf, M. Delcey, L. De Vico, W. Dobrautz, S. Dong, R. Feng, N. Ferré, M. Filatov(Gulak), L. Gagliardi, M. Garavelli, L. González, Y. Guan, M. Guo, M. Hennefarth, M. Hermes, C. Hoyer, M. Huix-Rotllant, V. Jaiswal, A. Kaiser, D. Kaliakin, M. Khamesian, D. King, V. Kochetov, M. Krośnicki, A. Kumaar, E. Larsson, S. Lehtola, M. Lepetit, H. Lischka, P. López Ríos, M. Lundberg, D. Ma, S. Mai, P. Marquetand, I. Merritt, F. Montorsi, M. Mörchen, A. Nenov, V. Nguyen, Y. Nishimoto, M. Oakley, M. Olivucci, M. Oppel, D. Padula, R. Pandharkar, Q. Phung, F. Plasser, G. Raggi, E. Rebolini, M. Reiher, I. Rivalta, D. Roca-Sanjuán, T. Romig, A. Safari, A. Sánchez-Mansilla, A. Sand, I. Schapiro, T. Scott, J. Segarra-Martí, F. Segatta, D. Sergentu, P. Sharma, R. Shepard, Y. Shu, J. Staab, T. Straatsma, L. Sørensen, B. Tenorio, D. Truhlar, L. Ungur, M. Vacher, V. Veryazov, T. Voß, O. Weser, D. Wu, X. Yang, D. Yarkony, C. Zhou, J. Zobel, and R. Lindh, "The OpenMolcas Web: A Community-Driven Approach to Advancing Computational Chemistry," *Journal of Chemical Theory and Computation*, 2023.

[157] J. Guthmuller, "Assessment of TD-DFT and CC2 methods for the calculation of resonance Raman intensities: application to *o*-nitrophenol," *Journal of Chemical Theory and Computation*, vol. 7, no. 4, pp. 1082–1089, 2011.

Acknowledgement

All the studies in this thesis were carried out under Professor Tetsuya Taketsugu, Department of Chemistry, Faculty of Science, Hokkaido University. I would like to express my sincere gratitude to Professor Tetsuya Taketsugu, for continuous advice, discussions, and generous help.

I would like to express my special thanks to Specially Appointed Assistant Professor Kenichiro Saita and Assistant Professor Takuro Tsutsumi for their all help and support on my researches.

I would like to express my appreciation to Professor Junya Hasegawa, Professor, Satoshi Maeda, Associate Professor Masato Kobayashi, Associate Professor Shinichiro Sato for serving on my doctoral thesis committee and for their constructive and insightfull suggestions.

I would like to offer my special thanks to former and present members of the Quantum Chemistry laboratory at Hokkaido University for advisable and practical discussions at our weekly seminar and/or small discussions in our student room.

All works in this thesis is supported by “The Hokkaido University Ambitious Doctoral Fellowship (Information Science/AI)” from MEXT and “the MEXT Doctoral program for DataRelated InnoVation Expert Hokkaido University (D-DRIVE-HU)”.

I would like to express my special thanks to “Ambitious program for smart materials

science (SMatS)" for providing some opportunities to learn different fields of study, mathematical science and data science, and more with those who major in different fields.

A part of the calculations in this thesis was performed using the Research Center for Computational Science, Okazaki, Japan. I would like to express my acknowledgement.

Finally, I would like to express my deepest gratitude to my family for their continuous support, especially for these six years of my research life.